Updraft Buoyancy within and Moistening by Cumulonimbi prior to MJO Convective Onset in a Regional Model

SCOTT W. POWELL

Department of Atmospheric Sciences, University of Washington, Seattle, Washington

(Manuscript received 30 October 2015, in final form 17 February 2016)

ABSTRACT

Processes responsible for widespread development of moderately deep cumulonimbi during a transition period before onset of two large-scale convective events associated with the Madden–Julian oscillation in late 2011 are investigated. A regional model (WRF) is capable of rapidly producing an approximately 3-day-long transition period prior to MJO convective onset similar to observed transition periods, during which moderately deep cumulonimbi were prevalent. During transition periods, evaporation in precipitating elements and horizontal advection of moisture away from the clouds in the nearby clear-air environment contributed to humidification below 400 hPa. Nonprecipitating clouds were present in the model mostly between 900 and 950 hPa and had no major impact on tropospheric moistening. Whether nonprecipitating cumuli grew into moderately deep cumulonimbi largely depended on the buoyancy of updrafts that extended into the 700–850-hPa layer. As mean environmental temperatures decreased, the mean cumulus updraft buoyancy in this layer became less negative. The start of two simulated transition periods were marked by rapid decreases in environmental temperature caused by reduction in environmental subsidence and/or increased cooling by advection or radiation. Small, widespread changes in the difference between 700- and 850-hPa environmental and updraft temperatures—on the order of 0.1 K and less than 0.4 K—had important ramifications for whether shallow clouds grew vertically into moderately deep clouds that moistened the troposphere and made it conducive to MJO convective onset.

1. Introduction

A satisfactory explanation for the cause of the Madden–Julian oscillation (MJO; Madden and Julian 1971, 1972) has long been elusive. Many theories have been proposed [summarized by Zhang (2005) and Wang (2011)] to explain how convective onset associated with an MJO event occurs over the Indian Ocean or tropical west Pacific and how the convection propagates. However, none have successfully generalized the dynamics governing the convective onset. The Dynamics of the Madden–Julian Oscillation field campaign (DYNAMO; Yoneyama et al. 2013), conducted over the Indian Ocean from late 2011 to early 2012, sought to elucidate the physical mechanisms governing onset and propagation, but particularly those involved in convective onset. Extensive radar and rawinsonde datasets, as well as ship-based near-surface ocean data and estimated surface fluxes, were obtained. Through many papers already published since DYNAMO, the observations have helped describe the behavior and evolution of convection during convectively active and suppressed periods. They have also helped to begin solidifying ideas of how onset of several MJO convective events occurred over the Indian Ocean.

Two major types of hypothesized mechanisms for MJO convective onset were prevalent before DYNAMO and remain so currently. The first type presumes that convection responds to some external forcing. For example, convection might be excited by extratropical disturbances that transport energy equatorward (Hsu et al. 1990; Ray and Li 2013; Zhao et al. 2013). Another prominent idea is that equatorial waves promote or suppress convection by altering the large-scale environment to make it more or less conducive to deep, moist convection. For many MJO convective outbreaks, the upward branch of a globally circumnavigating

Corresponding author address: Scott W. Powell, Department of Atmospheric Sciences, University of Washington, Box 351640, Seattle, WA 98195.
E-mail: spowell@atmos.uw.edu

DOI: 10.1175/JAS-D-15-0326.1

Kelvin-like wave approached the Indian Ocean as deep convection broke out (Knutson and Weickmann 1987; Gottschalck et al. 2013). Circumnavigating features of anomalous zonal wavenumber-1–1.5 velocity potential (Gottschalck et al. 2013) and vertical velocity (Powell and Houze 2015a) continuously circled the globe during DYNAMO, and Powell and Houze (2015a) proposed a possible mechanism relating the anomalous upward motions (associated with negative velocity potential anomalies) detected in reanalysis to MJO convective onset. Specifically, they showed how a small reduction in large-scale subsidence throughout the troposphere on the order of 0.01 Pa s^{-1} acted to cause a slight increase in the lapse rate below 500 hPa prior to MJO convective onset, which made the environment more favorable for development of moderately deep cumulonimbi. The moderately deep convection then moistened the middle troposphere and apparently offset some of the destabilization, the former of which is essential to formation of deep convection because deep convection is highly sensitive to low- and midtropospheric moisture (e.g., Derbyshire et al. 2004; Kuang 2010; Wang and Sobel 2012; Takemi 2015). Maloney and Wolding (2015) recently demonstrated that the amplitude of the MJO in their aquaplanet simulation was dependent upon the location of the upward branch of a circumnavigating Kelvin wave in their model; however, the realism of the interaction between the simulated Kelvin wave and MJO convection was unclear.

The second type of mechanism invokes processes local to the region where widespread convection eventually breaks out. Essentially, heat and moisture fluxes from the warm ocean, which gradually gets warmer during convectively suppressed periods, support shallow convection, which over time gradually moistens the lower to middle troposphere. The idea that a slow buildup in column-integrated moist static energy occurs over the Indian Ocean/tropical west Pacific prior to MJO convective onset was introduced by Bladé and Hartmann (1993) as the recharge component of ''discharge–recharge'' and has since been interpreted as a gradual (10–20 day) positive feedback between cumulonimbus depth and tropospheric humidity (e.g., Benedict and Randall 2007). However, the time scale of convective buildup during DYNAMO (the time between highly suppressed conditions and a convectively active MJO) was found using radar observations to be 2–8 days (Powell and Houze 2013, 2015b), a transition period during which the cloud population was characterized by a large number of moderately deep (~5 km) cumulonimbi. There is no reason yet, however, to believe that both of the above mentioned types of processes do not play some combined role in the observed onset cases.

Rawinsonde-based budget analyses of heat and moisture have been computed for DYNAMO at 1° spatial resolution (Johnson et al. 2015; Ciesielski et al. 2014). They are useful tools for determining the contribution to tropospheric moistening by processes on a scale smaller than the grid spacing of the sounding network. Ruppert and Johnson (2015) and Powell and Houze (2015a) both concluded that apparent processes on scales smaller than 1° (e.g., cloud processes) were responsible for most of the moistening during the 2–8-day transition period prior to two MJO onsets during October and November 2011. Both types of mechanisms for MJO convective onset mentioned above require moistening of the lower to middle troposphere, and DYNAMO observations show definitively that clouds are involved in that moistening process. However, without cloud-permitting model experiments to supplement the spatially coarse observational dataset, determining how much moistening occurred as a result of net upward transport of water vapor by clouds and how much can be attributed to evaporation in or near clouds is difficult.

Some attempts at modeling the observed MJO cases during DYNAMO at ''cloud permitting'' scales have already been made. For example, Hagos et al. (2014b) conducted a 2-month-long simulation over the Indian Ocean with 2-km horizontal grid spacing using the Weather Research and Forecasting (WRF) Model (Skamarock et al. 2008). Their simulation produced excessive precipitation in general but roughly captured the above referenced two eastward-propagating convective events as well as the suppressed period between them. The transition from shallow cumuli to deep cumulonimbi in their simulations took less than 6 days. The transition was highly sensitive to large-scale midtropospheric relative humidity, which itself was mostly controlled by large-scale vertical advection of moisture and meridional moisture advection. Ulate et al. (2015) ran numerous regional simulations with WRF at 1° horizontal resolution to test the impact of multiple forcing variables on the realism of their simulated MJO events. They found that the environmental humidity forcing was most important for a realistic simulation. Because clouds are essential for tropospheric moistening, their results suggest that whether the model produced widespread cloudiness depended primarily on whether the humidity in the boundary conditions forced the model to do so. Wang et al. (2015b) employed WRF to simulate the same MJO events as Hagos et al. (2014b). They used a horizontal grid spacing of 9 km after nudging horizontal winds to reanalysis for the first 3 days of their simulation. Their latitudinally averaged precipitation agreed extremely well with satellite-based estimates of precipitation. While they did not use a

cumulus parameterization, they still reproduced onset and propagation of two MJO convective events, but their resolution was too coarse to represent most vertically growing clouds. Aside from DYNAMO, Chikira (2014) integrated a global climate model over 15 yr with the cumulus parameterization of Chikira and Sugiyama (2010) to model MJO activity. Among other findings, he concluded that clouds are important elements for moistening via vertical motion. He noted that the enhancement of congestus cloudiness during the MJO mature phase was favored by a ''marginally unstable'' environment even over the large-scale convective center but did not further explore the evolution of tropospheric static stability as the cloud population evolved into deep, widespread cloud systems.

Based on the above results, the importance of a transition period during which moderately deep cumulonimbi, but not deep clouds, are numerous is obvious. Some key questions concern how the transition period develops and why the evolution of the cloud population into such a transition period can occur rapidly—over as little as a couple of days as observed by Powell and Houze (2015b). Ultimately at the scale of individual cloud updrafts, buoyancies within the parent clouds' environments determine the depths of the clouds, and so the problem of MJO convective onset might be partially simplified to determining what factors control changes in the large-scale mean buoyancy of cumulus/cumulonimbus updrafts on time scales relevant to MJO variability. Three modes of cloud depth have been observed in the tropics (Johnson et al. 1999; Hollars et al. 2004; Posselt et al. 2008): a shallow nonprecipitating mode, a moderately deep congestus/moderately deep cumulonimbus mode, and a deep cumulonimbus mode. Zuidema (1998) documented a minimum in tropical cloudiness between 600 and 800 hPa, or between the tops of the shallow and medium modes. The minimum is linked to a climatological increase in mean atmospheric stability above the nonprecipitating cloud layer. Less stable regions are present above and below the relatively stable layer. Updrafts with enough buoyancy to penetrate the stable layer encounter a layer of decreased stability between about 600 and 700 hPa and can continue rising to the next stable layer near the 0°C level to become moderately deep. Those clouds that can penetrate the 0°C stable layer, barring entrainment of dry air or other processes that would negatively impact updraft buoyancy, can rise freely to the tropopause and become deep cumuli/cumulonimbi. The mean lapse rate profile over the Indian Ocean during DYNAMO contains the same stable and conditionally unstable layers at similar levels as reported by Zuidema (Powell and Houze 2015a). A key question addressed by this article concerns how and when shallow, often nonprecipitating, convection more frequently grows to penetrate the 600–800-hPa stable layer and become moderately deep convection, thus marking the beginning of a transition period into MJO convective onset.

In this article, we will use a regional model configuration similar to that used by Hagos et al. (2014b) to explore the evolution of the cloud population prior to two MJO events in greater detail than can be done with observations alone. Specifically, our objectives are to determine

1) the sources of moisture that are important for the onset of transition periods prior to MJO convective onset,
2) whether total advection of vapor or evaporation within clouds is primarily responsible for midtropospheric moistening during transition periods,
3) the model's representation of the role of shallow nonprecipitating convection in moistening the environment prior to MJO convective onset, and
4) factors that impact cloud updraft buoyancy in a stable layer above the boundary layer such that moderately deep convection is more frequently permitted.

2. Model description

We employed version 3.5.1 of the nonhydrostatic WRF Model. Our domain was centered over Gan Island (0.69°S, 73.15°E) and was 3280 km (zonally) × 2240 km (meridionally). The yellow box in Fig. 1 outlines the full model domain. Horizontal grid spacing was 2 km, and 38 vertical levels, equally spaced in WRF eta (η) coordinates, were used. The model top was 50 hPa. The European Centre for Medium-Range Weather Forecasts (ECMWF) interim reanalysis (ERA-Interim; Dee et al. 2011) with 0.75° horizontal grid spacing was used for initial and lateral boundary conditions. Boundary forcing was linearly interpolated to the model state every 6 h within eight grid points of the lateral boundaries. Sea surface temperatures (SSTs) were updated daily with the real-time high-resolution global sea surface temperature (RTG_SST_HR) analysis (http://polar.ncep.noaa.gov/sst/rtg_high_res/description.shtml), which is provided at $^1/_{12}$° spacing. The daily SSTs were interpolated between values available at 0000 UTC so that forcing was available to the model every 6 h. Physics packages employed were Thompson microphysics (Thompson et al. 2008), the GCM version of the Rapid Radiative Transfer Model (Iacono et al. 2008), the Mellor–Yamada–Janjić (MYJ; Janjić 1994) planetary boundary layer (PBL) scheme, the unified Noah land

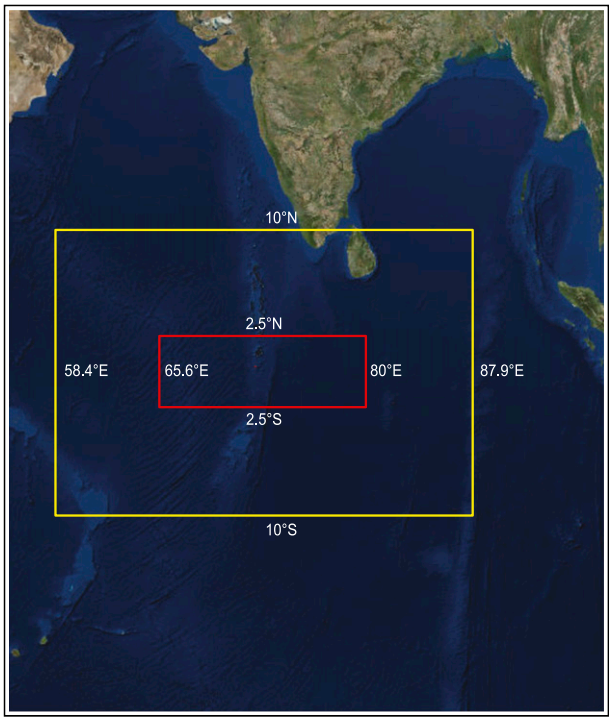

FIG. 1. Map of the Indian Ocean containing the WRF Model domain (yellow box), bounded by 9°N–9°S and 58.4°–87.9°E. The subdomain (red box) in which analysis in this article is performed is bounded by 2.5°N–2.5°S and 65.6°–80°E. The subdomain is henceforth in the text referred to as the domain.

surface model (Tewari et al. 2004), and Monin–Obukhov similarity for the surface layer. Prior studies (e.g., Powell et al. 2012; Hagos et al. 2014a; Rasmussen and Houze 2016) have shown that Thompson microphysics satisfactorily represent the structure of mesoscale convective systems and their anvil clouds; although many microphysics parameterizations, including Thompson's, exhibit a high bias in cloud depth (Hagos et al. 2014a; Wang et al. 2015a). The MYJ PBL scheme is used because it demonstrates the smallest positive precipitation bias over the Indian Ocean from available options (L. Berg 2014, personal communication). Output, including moisture tendencies due to phase changes, is written every 3 h. To permit model spinup, the first 24 h of output is not used in the following analysis.

We simulated the transition into two MJO convectively active events over the Indian Ocean. MJO convective onset was observed to occur near the equator during the middle of October and November 2011 (Johnson and Ciesielski 2013; Powell and Houze 2013; Xu and Rutledge 2014). To capture the transition period prior to onset for both cases, we initialized the model during suppressed periods prior to each event. The initial dates for the two runs were 1 October and 4 November. They were integrated with a 12-s time step for 19 and 16 days, respectively. The results presented in this paper are obtained from a subdomain (henceforth referred to as the domain) near the equator bounded by 2.5°N–2.5°S and 65.6°–80.0°E and outlined by the red box in Fig. 1. Mesoscale convective systems (MCSs) were often present in the southernmost part of the yellow box, and choosing an equatorially confined domain isolates our analysis (which is focused before MJO convective onset) to almost exclusively small and/or isolated convective elements that do not develop expansive stratiform precipitation regions.

3. Comparison to observations and reanalysis

Domain-averaged relative humidity (RH) for both simulations is depicted on the top row of Fig. 2. RH exceeds 80% at all levels below 900 hPa at most times during both control simulations. In October (Fig. 2a), RH from 400 to 800 hPa rapidly increases from 30%–40% to 70%–80% around 10–13 October. A less pronounced increase in RH at the same levels—from 40%–50% to 70%–80% occurs between 9 and 13 November (Fig. 2b). The apparent stepwise increase in moisture—first up to around 400 hPa, then to the tropopause—is especially prominent in October and is consistent with that first reported for these cases by Johnson and Ciesielski (2013). A diurnal cycle also appears in the RH field between 950 and 850 hPa prior to the humidity buildup periods and is likely related to shallow convection (Ruppert and Johnson 2015).

Mean RH profiles derived from ERA-Interim [shown to be consistent with rawinsonde humidity profiles in a similar domain by Powell and Houze (2015b)] within the simulation domain are illustrated in Fig. 2c (for October) and Fig. 2d (for November). In general, the simulated RH in October agrees with reanalysis profiles; however, the model is too dry through the depth of the troposphere prior to 12 October. The depth of the 60% RH contour increases on 12 October in both the model and reanalysis. However, the simulated moistening between 850 and 500 hPa appears to occur more rapidly than in reanalysis. Prior to 12 November, the simulated RH is again often lower than reanalysis values, and the model does not reproduce a short rain event that was observed during 9–10 November. Between 11 and 17 November, the model is excessively moist, particularly above 500 hPa. However, the timing of the rise in the depth of the 60% contour in the model again agrees with reanalysis, occurring on 11 November for both. The latter detail is important because it means that the buildup of humidity in WRF occurs at approximately the correct time in both simulations.

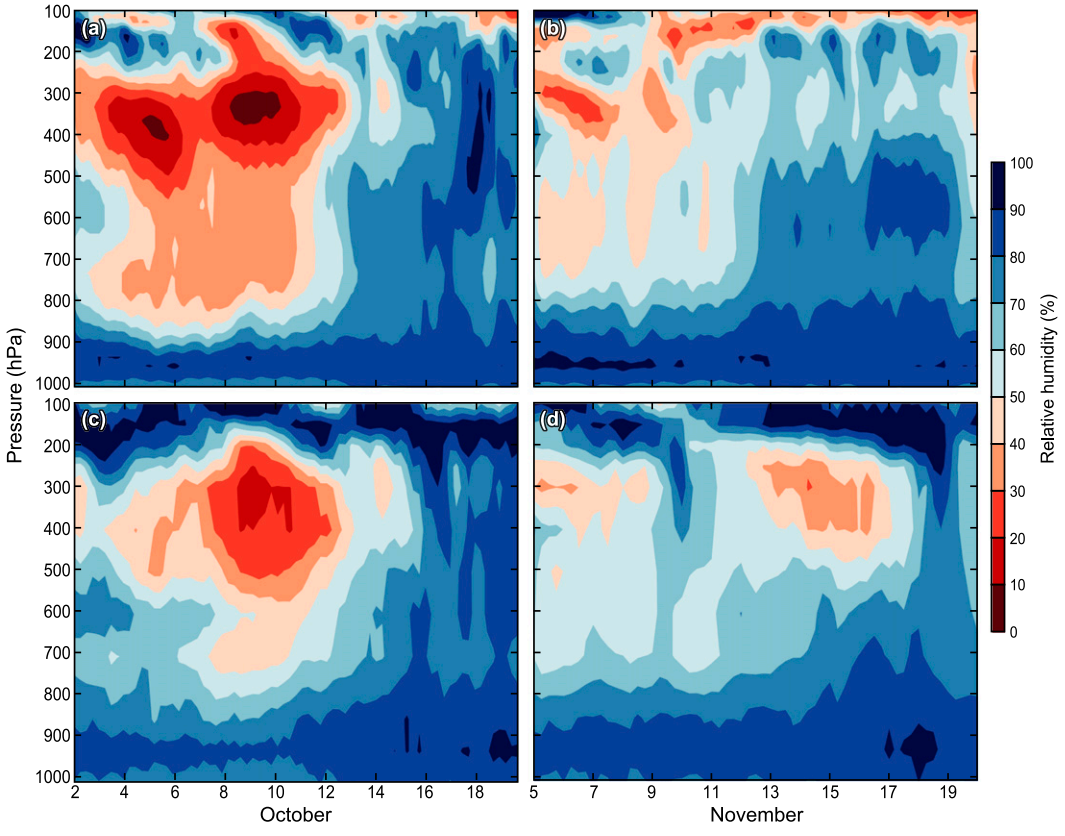

FIG. 2. Time series of simulated domain-mean relative humidity for (a) 2–20 Oct and (b) 5–20 Nov. (c),(d) As in (a) and (b), respectively, but using ERA-Interim.

Simulated domain-mean profiles of zonal (Figs. 3a,b) and meridional (Figs. 4a,b) wind in October (left panels) and November (right panels) are similar to those computed over the same domain using ERA-Interim (Figs. 3c,d and 4c,d). Only occasional slight differences between simulated and reanalysis zonal or meridional wind are present during either month. Given the regional size of our domain and that the simulation was periodically forced by ERA-Interim, this is not surprising, but it is indicative that the model reproduced features of the large-scale circulation that were present during DYNAMO. The similarity between large-scale ERA-Interim fields and point observations during DYNAMO was established in Powell and Houze (2015b).

The October simulation produced a time series of domain-mean precipitation rate that was closer to observed rates than the November simulation. Figure 5 illustrates domain-mean rain rates computed over the same area (red box in Fig. 1) and times using simulations (black) and the Tropical Radar Measurement Mission (TRMM) 3B42 (Huffman et al. 2007) dataset (magenta). Rain rates from the ground-based S-Ka band dual-wavelength, dual-polarimetric (S-PolKa) radar, whose observational domain spanned about 10% of the area of the model domain utilized for analysis, are shown in blue. In October (Fig. 5a), observed rain rates began to increase from near zero on 10 October (S-PolKa) or 11–12 October (TRMM). Simulated rain rate began to increase on 10 October, but by 13 October, the model was precipitating excessively. Then, the model failed to reproduce the high rain rates observed during observed convectively active periods after 15 October. In November (Fig. 5b), an increase in precipitation was observed on 9–10 November. S-PolKa (blue) detected significantly more intense precipitation than TRMM on 11–12 November, suggesting that the rain S-PolKa observed was not representative of conditions within a wider domain on those days. The model produced increasing rain rates when observed rain rates rose on 9 November, but the model rained excessively from 13 to 16 November. Again, the simulated domain-mean during the most convectively active day in observations (18 November) was much less than observed rain rates. The simulations were effective at reproducing the onset of enhanced rainfall that occurs near the beginning of observed transition

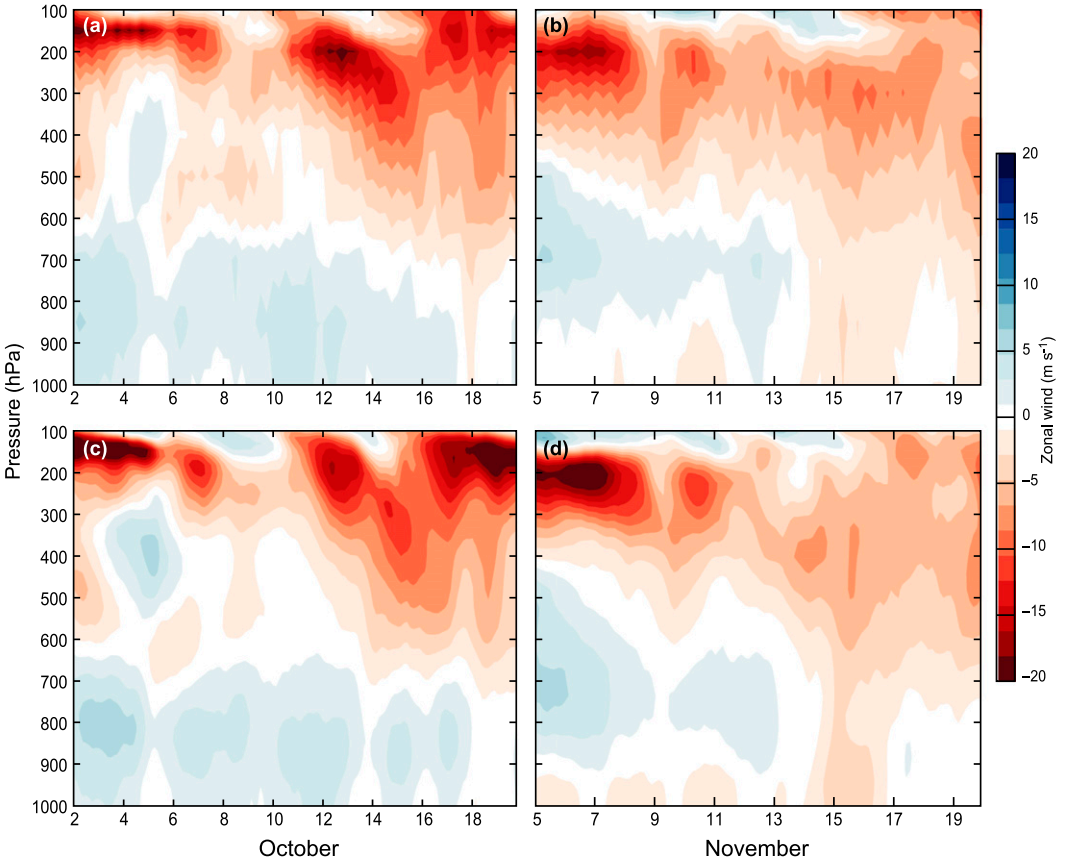

FIG. 3. As in Fig. 2, but for zonal wind.

periods, but the model transitioned into convectively active conditions too quickly in each simulation, and the model could not reproduce the largest rain rates observed during active periods. Part of the latter issue may simply be related to the exact timing and location of convection within our domain, but it may also be a consequence of using coarse horizontal resolution (4 km^2) that does not completely resolve the most intense cloud updrafts.

Figure 6 is a time series of histograms of 20-dBZ echo-top heights for deep and shallow convective precipitating grid columns during each control simulation. Grid columns were separated into convective and stratiform elements using the simulated reflectivity exactly following Powell et al. (2016). Simulated reflectivity was calculated during model integration using an S-band radar simulator coded by U. Blahak and implemented into WRF by G. Thompson. The 20-dBZ echo tops seldom appeared during suppressed periods prior to 8 October and 9 November, but brief exceptions occurred on 6 October and 6 November. A rapid increase in the number of 20-dBZ echo tops between 3 and 8 km occurred on 8 October and 9 November. On 12 October and 12 November, 20-dBZ echo tops between 8 and 10 km and as high as 14–16 km became prevalent. The periods during which >20-dBZ echo-top heights between 3 and 8 km were prevalent in the absence of deeper convection are denoted as transition periods along the top abscissa of Fig. 6 and all subsequent figures with time on the abscissa. They were preceded (followed) by suppressed (active) periods.

Compared to TRMM radar observations over a larger domain (Powell and Houze 2015b), the simulated echo tops were systematically too high. Particularly, during transition periods, observed 20-dBZ echo tops above 5 km were rare. Such a bias in modeled echo tops is also apparent in similar studies (Hagos et al. 2014a; Wang et al. 2015a). Model reflectivity, though, was simulated for the S-band frequency, and the echo-top height distribution from S-Polka was similar to that seen by TRMM but shifted upward about 1–2 km (Powell and Houze 2015b), so some bias is expected. A direct comparison of simulated echo-top heights to those observed by S-PolKa, however, is difficult because of the latter's small domain. Compared to TRMM and ground-based radar observations, and as seen above in Fig. 6, the

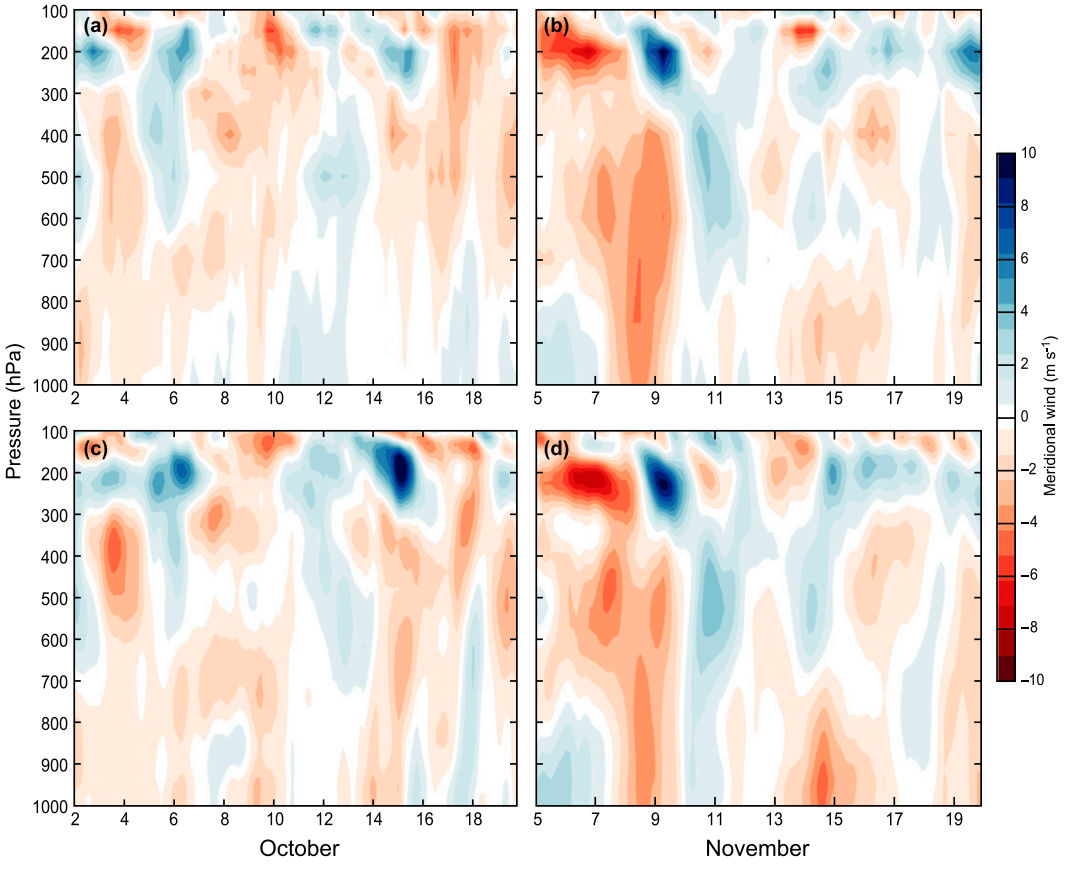

FIG. 4. As in Fig. 2, but for meridional wind.

transition periods started at the correct times but are about 3–4 days too short. Nonetheless, and most importantly for this study, the model produced a distinct transition period prior to MJO convective onset, and the evolution of RH at the onset of transitions (Fig. 2)—both in terms of its time scale and depth—was similar to that seen in observations. Thus, our simulated MJO transition periods are not perfect representations of the real events, but they are realistic enough to explore the mechanisms responsible in WRF for their development prior to MJO

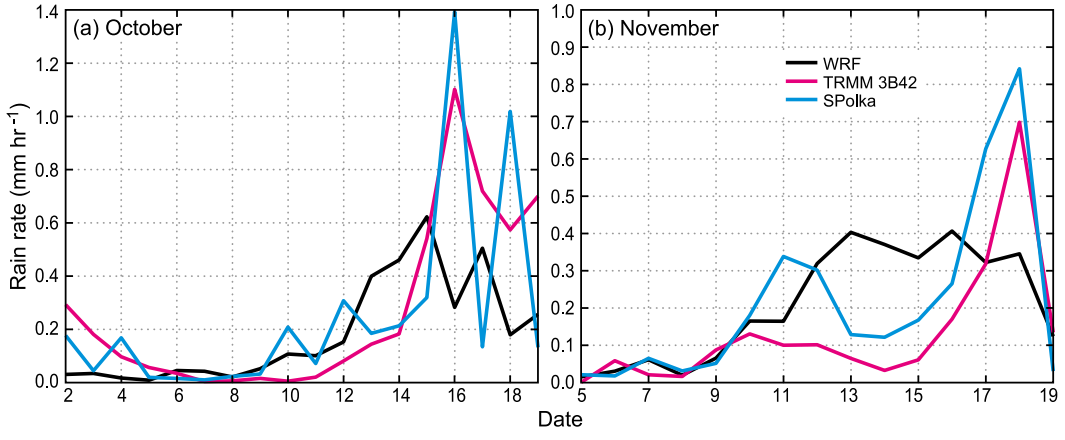

FIG. 5. Time series of simulated domain-mean rain rate (black) during the (a) October and (b) November simulations. Observed rain-rate estimates from TRMM 3B42 within the same domain are shown in magenta. Rain rates derived from S-PolKa radar data are displayed in blue.

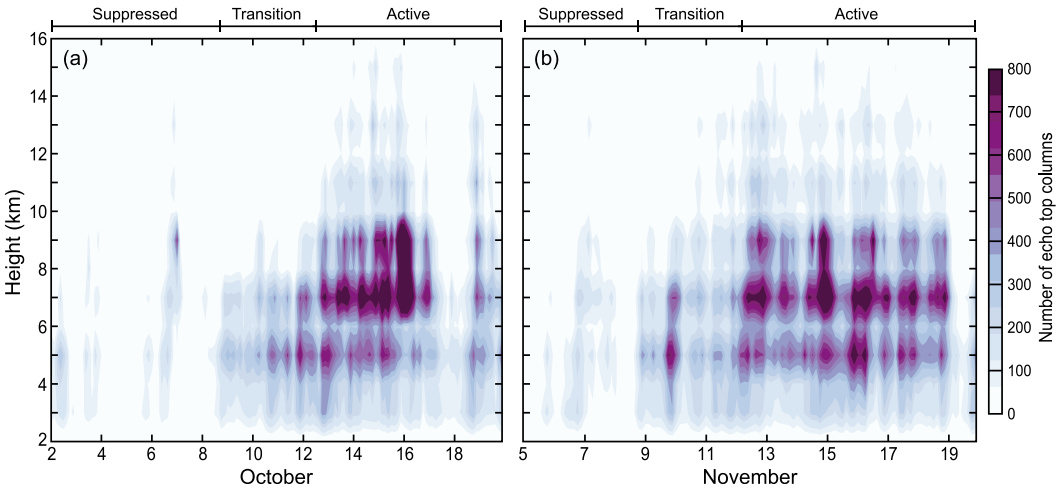

FIG. 6. Time series of the histogram of simulated 20-dBZ echo-top heights from (a) 2–20 Oct and (b) 5–20 Nov. Suppressed, active, and transition periods are denoted along the top abscissa here and in later figures. These periods are described in the text.

onset and the roles played by shallow and moderately deep convection in tropospheric moistening during transition periods.

4. Calculating moisture tendencies from model output

In section 5, we will investigate moisture sources and sinks into and out of the analysis domain. At each model output time, the total tendency of water vapor mass in the domain was, using available model parameters,

$$\frac{\partial[m_w]}{\partial t} = \sum_k \left(\langle u^k_{b,x} \rangle q^k_{b,x} \frac{dP^k_{b,x}}{g} dx + \langle v^k_{b,y} \rangle q^k_{b,y} \frac{dP^k_{b,y}}{g} dx + E_{\text{sfc}} + [M^k] \right), \quad (1)$$

in which k (not an exponent) represents the set of all vertical levels, m_w is the water vapor mass in the domain, u and v are zonal and meridional winds, respectively, q is specific humidity, dP is the difference in pressure between the bottom and top of each grid box, dx is the horizontal grid spacing, E_{sfc} represents total evaporation of surface moisture in the domain, and M is the total tendency in each grid box due to phase changes. Angle brackets indicate that the value is on a grid that is staggered with the grid on which q is outputted; therefore, such values sit on the domain boundary. Square brackets indicate a total summed over all grid locations in the domain. A subscript b indicates that only values on the lateral boundaries of the domain are considered, and subscripts x or y indicate, respectively, whether such values are considered along the west/east boundary or along the north/south boundary. For q_b, the value just inside (outside) the domain is used if the horizontal flow is out of (into) the domain. The value for dP_b just within the domain boundary is always used. Combined, the first two terms of Eq. (1) describe the change of water vapor mass attributed to horizontal flux of vapor through the lateral domain boundaries. Because Eq. (1) is a summation, it is, of course, highly sensitive to domain size and is intended to highlight relative magnitudes of each term rather than absolute differences between them.

Section 6 explores the moisture tendency inside individual grid boxes. In each grid box, the vapor mass tendency is defined as

$$\frac{\partial m_{\text{grid}}}{\partial t} = -\frac{dP}{g} dx^2 (\mathbf{u} \cdot \nabla q) + M, \quad (2)$$

in which m_{grid} is the mass of water vapor in a grid box and $\mathbf{u}$ is the vector wind on the six faces of each box. The first term in Eq. (2) can be decomposed into three terms that include moisture tendencies caused by apparent horizontal and vertical advection of moisture.

5. Moisture sources/sinks in the domain

Figures 7a and 7b contain time series of total moisture tendency ($\partial[m_w]/\partial t$) due to phase changes (magenta), horizontal fluxes of moisture across lateral boundaries (blue), and surface evaporation (gray) for both control simulations. The black line represents the sum of all terms in Eq. (1) and the green line depicts the sum of horizontal flux and phase-change terms, which largely offset when convection was common. The total moisture tendency in the domain was negative for the first few

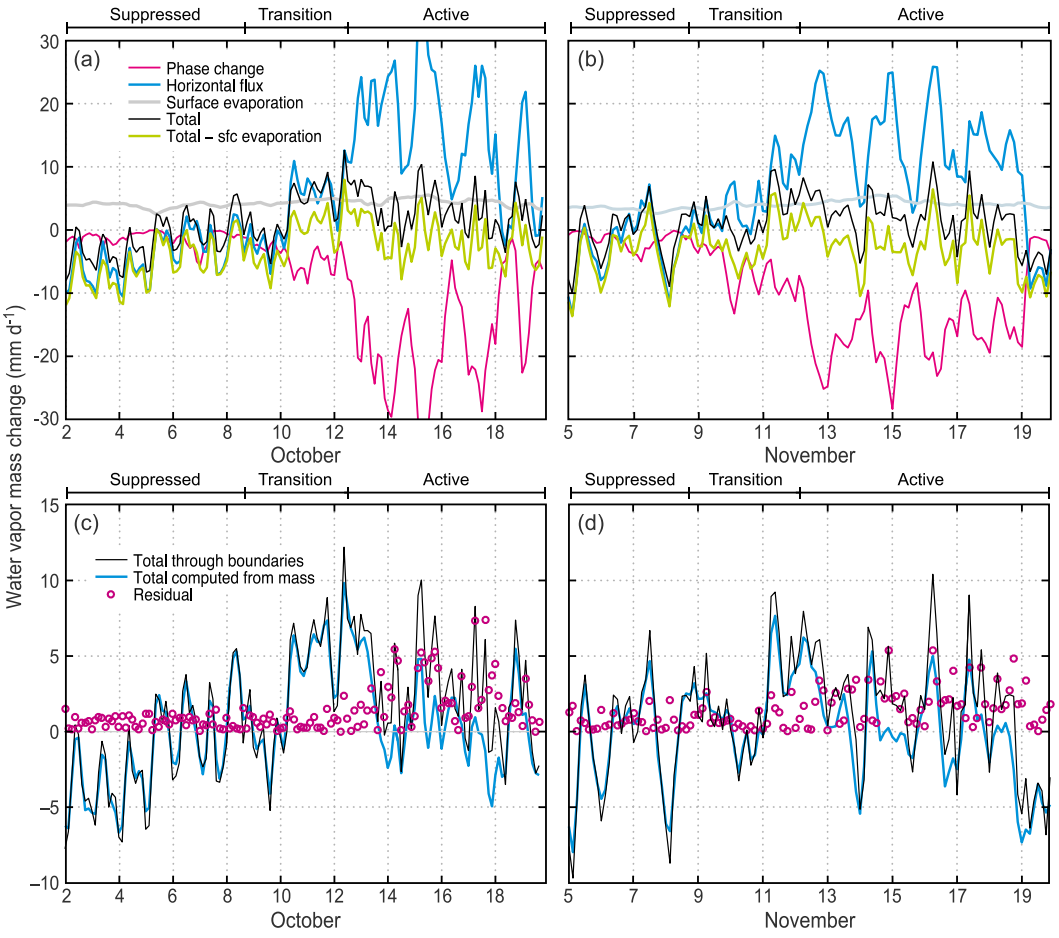

FIG. 7. (top) Time series of contributions to the total domain water vapor mass tendency by phase changes (magenta), horizontal fluxes through the domain boundaries (blue), surface evaporation (gray), the total of all terms (black), and the total minus surface evaporation (green) for (a) October and (b) November. (bottom) For (c) October and (d) November, the domain water vapor mass tendency calculated using first-order centered differencing in time (blue) and instantaneous values (black) as shown in (a) and (b). Magenta circles represent the magnitude of the difference between the two lines.

days of the October simulation as moisture was fluxed out of the domain. The same occurred more periodically during the suppressed period in the November simulation. Then, the moisture tendencies became persistently positive for more than a day 1–2 days after the beginning of the transition periods for each simulation. Variability in the domain moisture tendency was dominated by the relatively small imbalance between large horizontal flux and phase-change terms. Relative to the other terms, domain-mean surface moisture flux was approximately constant ($4\,\mathrm{mm\,day^{-1}}$ or about $115\,\mathrm{W\,m^{-2}}$); although locally, it is known to have varied significantly from its own mean during periods of high surface wind speed (Ruppert and Johnson 2015; de Szoeke et al. 2015). The range of single-point modeled values (not shown) corresponded to latent heat fluxes of about $75–150\,\mathrm{W\,m^{-2}}$ and agrees favorably with retrievals of surface flux based on observations (Ruppert and Johnson 2015; de Szoeke et al. 2015). Horizontal flux and phase changes largely balanced each other (green lines near zero in Fig. 7) after the transition periods began, especially from 10 to 12 October, so their net effect to domain moistening was small. Thus, surface evaporation was essential for allowing domain-mean moistening (black lines greater than zero in Fig. 7) to occur. In summary, during transition and active periods, a major source of eventual cloud condensate was horizontal flux of moisture into the domain. At such times, when most of the vapor fluxed into the domain condensed inside clouds, the magnitude of the relatively constant domain-mean surface moisture fluxes often contributed largely to the total rate of moistening in the domain.

The values shown in Figs. 7a and 7b show instantaneous moisture tendencies every 3 h associated with the terms in

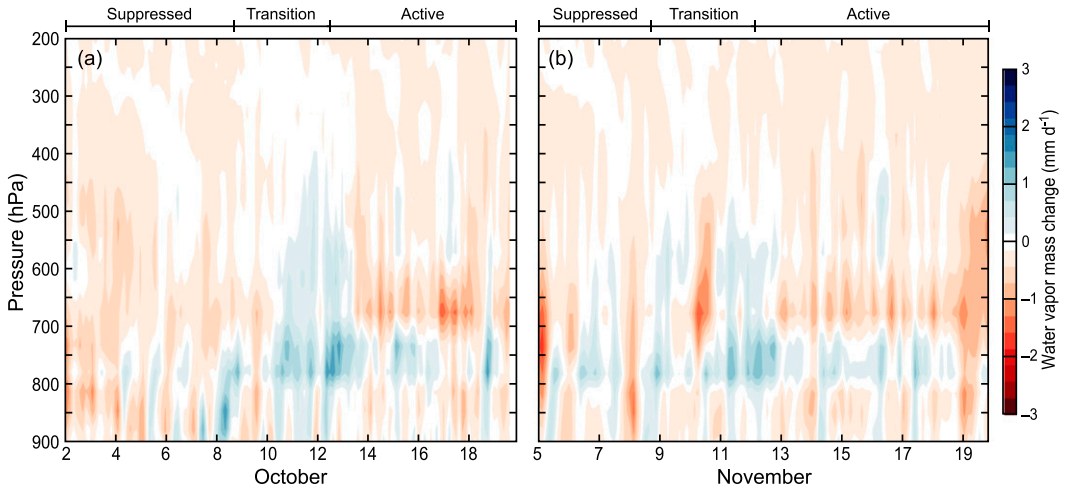

FIG. 8. Time series of mean domain water vapor mass tendency at model levels above 900 hPa for (a) October and (b) November.

Eq. (1). However can these tendencies be used to estimate the moisture flux into/out of the domain during 3-h-long periods; that is, are the tendencies too variable for instantaneous values to describe the evolution of humidity in the model? Figures 7c and 7d address this question. The black line is the same as that in Figs. 7a and 7b. The blue line represents estimates of the moisture tendency calculated using first-order centered differencing in time at each output time. Magenta circles depict the magnitudes of the residuals between the two. The residual is small compared to both estimates of the moisture tendency during suppressed and transition periods. The residual then becomes relatively large during active periods; however, this study is primarily focused on the evolution of the cloud population leading up to and during transition periods; results during active periods are shown for completeness.

6. Cloud contributions to vapor tendency

Above, we showed that net moistening of the model domain began during transition periods prior to MJO onset. Moderately deep cumulonimbus clouds (Fig. 6) redistributed that moisture vertically throughout the domain. In this section, we investigate the processes through which the environment was moistened. The total vapor tendency is primarily of interest at model levels above 900 hPa and is shown in Fig. 8 for the control simulations. In Figs. 8–10 (and later in Fig. 12), the values of interest are separately averaged within the domain at each model level, creating a vertical profile of domain means at each model output time. The values referenced below depict means at individual levels, not the cumulative sums of means across the several model levels. In October, moistening occurred for a short period between 750 and 900 hPa on 8 October. It was followed by a period of drying, then a longer period of moistening on and after 10 October between 400 and 900 hPa with an apparent maximum between 700 and 800 hPa often exceeding 1 mm day^{-1}. During the suppressed period in November, moistening occurred on 6–7 November below 500 hPa but was followed by strong drying between 600 and 700 hPa on 8 November. Moistening up to 500 hPa started on 9 November, was interrupted by drying as large as −2 mm day^{-1} in the 500–700-hPa layer on 10 November, and then persistent moistening occurred between 500 and 800 hPa from 11 to 13 November. During both simulations, moistening was prevalent between 700 and 800 hPa even after the cloud population completes the transition into larger deep systems.

We separated grid cells into four categories that are roughly based on whether a cloud was present and the type of cloud that was present. Specifically, we categorize each model grid box as precipitating cloud, nonprecipitating liquid cloud, nonprecipitating ice cloud, or environment (no cloud). The separation is roughly based on the rain-type classification of Powell et al. (2016) in that any grid box with simulated reflectivity below (above) 7 dBZ is classified as nonprecipitating (precipitating). Nonprecipitating ice cloud is defined as having a temperature less than 0°C. All other grid boxes are classified as environment. Because ice clouds, by this definition, are restricted to above the 0°C level, their direct contributions to moistening are restricted to the upper troposphere and are of minimal importance to making the lower troposphere conducive to deep convection. We will focus on moisture tendencies associated with the other three categories throughout the remainder of this article.

For each category, moistening can be separated into vertical and horizontal advective components and the vapor tendency due to phase changes following Eq. (2), generating a total of nine terms. Five of those terms dominate the vapor tendency: vertical and horizontal advection and phase changes in precipitating elements and vertical and horizontal advection in the environment. Figures 9 and 10 illustrate the time series of total moistening at each level attributed to some of the large terms for the October and November control simulations, respectively. Vertical advection of moisture and phase changes both contributed to large, but oppositely signed moisture tendencies that largely balanced each other and are not displayed. Horizontal advection of moisture (Figs. 9a and 10a) in precipitating elements was generally negative with magnitudes less than 1 mm day^{-1}. During suppressed and transition periods it was slightly positive between 750 and 850 hPa and slightly negative above 750 hPa. During active periods, the term was more negative, with magnitudes as large as 1.5 mm day^{-1} around 700 hPa. Figures 9b and 10b show the mean total moistening in precipitating elements. Vapor tendency due to processes within precipitating clouds was generally $\leq$1 mm day^{-1} at model levels below 500 hPa after the transition periods began, but it was positive, meaning that the net effect of phase changes did not remove all of the water vapor that was vertically fluxed upward. Some of the condensed water evaporated (Figs. 9c and 10c) and evaporation rates below 600 hPa during transition periods commonly ranged from 0.25 to 0.75 mm day^{-1}. Figures 9d and 10d represent the moisture tendency in precipitating elements attributed to vertical advection of moisture and phase changes minus that due to evaporation. They reveal that in-cloud vertical advection plus condensation had a net drying impact at almost all levels and all times. Thus, evaporation was the process through which precipitating elements directly contributed to a net moistening of the clear-air environment during transition periods. The moisture tendencies due to evaporation either reflect detrainment of vertically fluxed moisture into the cloud environment or dissipation of the cloud.

Positive vapor tendency due to horizontal advection of moisture in environmental grid boxes below 500 hPa was also important (Figs. 9e and 10e). Above 900 hPa in October, total domain-averaged moisture tendencies of 0.25–1.25 mm day^{-1}, generally decreasing with height, are depicted when moderately deep cumulonimbi were present during transition periods. In November, tendencies of $\leq$1 mm day^{-1} occurred. Vapor tendencies of up to 1.5 mm day^{-1} regularly occurred between 900 and 950 hPa during suppressed and transition periods. The moistening—particularly that above 900 hPa—was probably associated with divergent flow away from clouds and into the environment. Thus, while this moistening occurred outside of clouds, it is still probably attributed to cloud-scale dynamics, and should be considered part of the subgrid-scale apparent moistening (or the negative Q2 term) derived from sounding budget analysis by Ruppert and Johnson (2015) and Powell and Houze (2015a). As deep cumulonimbi became more prevalent during the middle of each month, horizontal vapor advection in the environment became slightly negative. This probably occurred because mesoscale convergence in the environment surrounding deep and large cloud systems followed the gradient of moisture from a dry environment to a saturated cloud; that is, dry environmental air converges into MCSs in the middle levels (Kingsmill and Houze 1999). Environmental subsidence (Figs. 9f and 10f) that compensated for cloud updrafts had a strong drying effect and an obvious diurnal signal during suppressed and transition periods during both October and November. Vapor tendencies were frequently between -1 and -2 mm day^{-1} between 800 and 900 hPa during October and 700 and 900 hPa during November, and the drying by compensating subsidence outside clouds extended as high as 400–500 hPa. Negative tendencies decreased in magnitude after the November transition period began. Because mean vertical motion in the clear-air environment was, of course, downward, weak drying via subsidence was nearly always experienced at all levels.

Figure 11 shows the mean magnitude of the environmental advective terms as a function of distance from the nearest precipitating cloud during transition periods only. Values are depicted at four discrete model levels in the lower half of the troposphere, and the average pressure along each level is noted in the legend. Solid (dashed) lines indicate horizontal (vertical) advection. Most importantly, the magnitude of either dramatically decreased within the first 6 km from a cloud. In October (Fig. 11a), horizontal advection in the grid boxes next to a cloud averaged between 2 and 3 mm day^{-1} below 620 hPa. The value approached an asymptote slightly above zero at distances above 6 km. In November (Fig. 11b), similar behavior was simulated, although the values approached zero at distances greater than 8–10 km at higher levels (green and black). Values of horizontal advection at 0–2 km in November were similar to or less than those at 2–4 km because an observed and simulated rain event developed in the domain around 10 November and was associated with negative horizontal advection of moisture (Fig. 10e), during the time period included in Fig. 11. Any differences in values across various levels at the same distance (e.g., the $\sim$7 mm day^{-1} horizontal advection at 479 hPa in October)

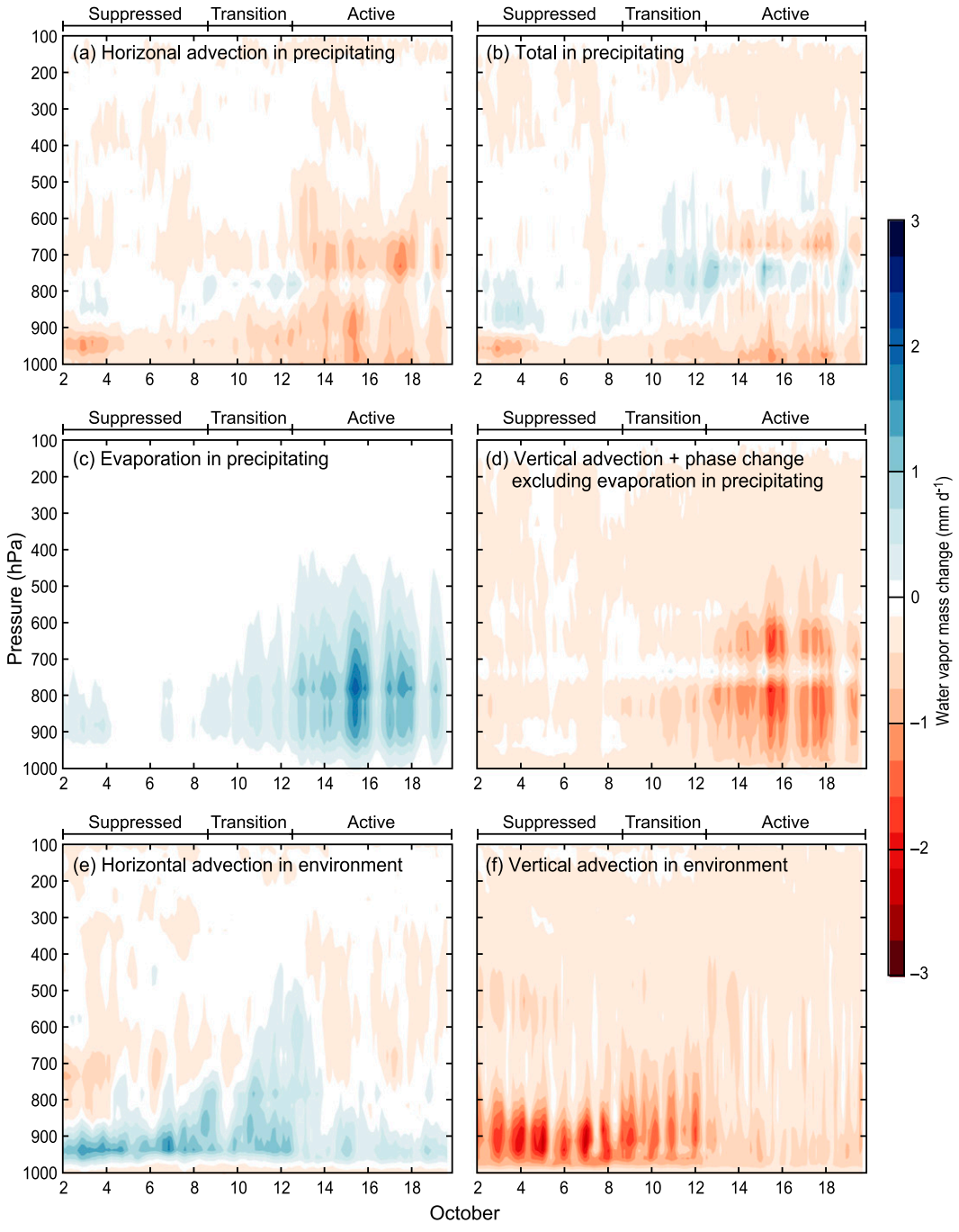

FIG. 9. Time series of the domain water vapor mass tendency attributed to mean (a) horizontal advection of water vapor within precipitating elements, (b) total tendency within precipitating elements, (c) evaporation within precipitating elements, (d) vertical advection plus phase changes minus evaporation within precipitating elements, (e) horizontal advection in environmental grid boxes, and (f) vertical advection in environmental grid boxes during October.

should not be interpreted as robust, reproducible results, but the systematic decrease of the values with distance at all pressure levels is important. Environmental subsidence drying (dashed lines) was also largest near clouds, and it approached zero at distances greater than 6 km from a cloud. Environmental subsidence drying at lower levels (magenta and blue) was around $-0.5\,\mathrm{mm\,day^{-1}}$ well away from a cloud.

Figure 12 is similar to Figs. 9 and 10, highlights the 800–1000-hPa layer, and depicts the total contribution

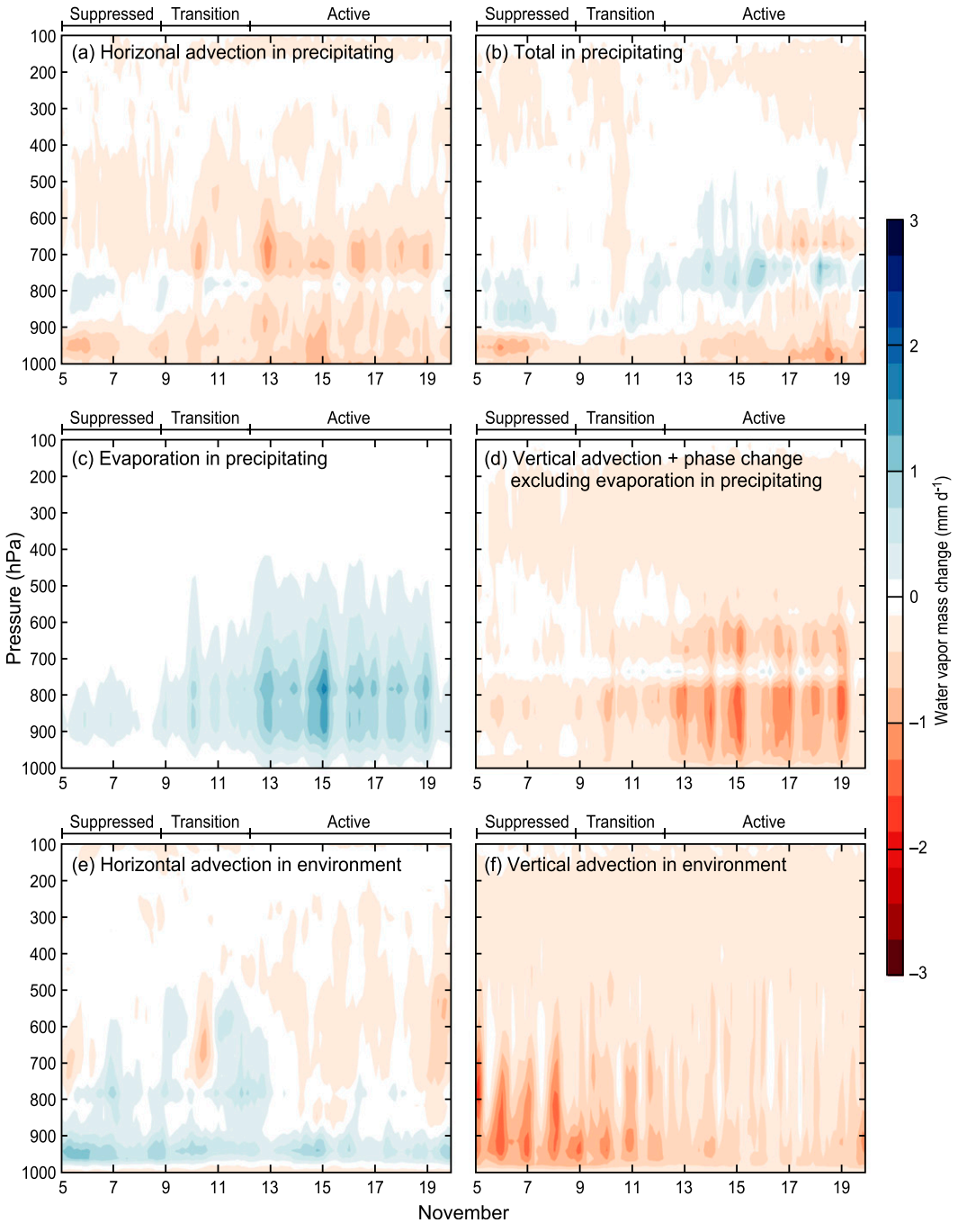

FIG. 10. As in Fig. 9, but for November.

to moistening within nonprecipitating clouds. Nonprecipitating clouds in WRF generally extended upward to around 880–900 hPa from their cloud base at the lifting condensation level, which remained around 950–970 hPa during both simulations. A vapor tendency as large as 0.5–0.6 mm day^{-1} was the same order of magnitude as the total tendency within precipitating elements below 900 hPa (Figs. 9b and 10b). However, compensating subsidence in the environment (Figs. 9f and 10f) offset some of the total contribution of the cumuli to total moistening. Figure 13 plots time series of the mean domain-mean vapor tendencies between three model levels (i.e., a mean of three domain means) from 900 to 950 hPa attributed to processes in nonprecipitating grid boxes (gray), the tendency caused by horizontal advection in precipitating elements (blue), the sum of the mean tendencies by vertical advection and

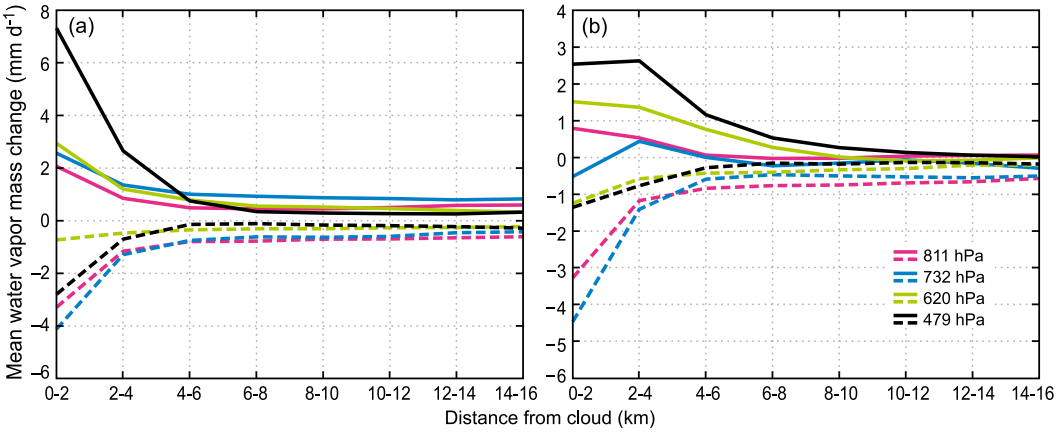

FIG. 11. Mean horizontal (solid) and vertical (dashed) advection of moisture in environmental grid boxes as a function of distance from a cloud at mean pressure levels (constant η levels in WRF) of 811 (magenta), 732 (blue), 620 (green), and 479 hPa (black).

phase changes in precipitating clouds (magenta), and total vapor tendency including that in environmental regions (black). As mentioned above, nonprecipitating elements always had a moistening effect; however, the moistening was countered primarily by drying by horizontal advection inside the lower portions of precipitating elements and environmental subsidence (Figs. 9f and 10f). The cumulative mean total vapor tendency (integral of black line) was very close to zero ($-0.007\,\mathrm{mm\,day^{-1}}$ in October and $0.015\,\mathrm{mm\,day^{-1}}$ in November) during both simulations, so while nonprecipitating clouds persistently acted to moisten the environment, their moistening impact was too small to have any major extended impact on the total moisture tendency experienced in the layer where the clouds persisted. This is consistent with observational results from Zermeño-Díaz et al. (2015), who concluded similarly that shallow (but not exclusively nonprecipitating) clouds had a constant but small moistening effect on the lower troposphere prior to MJO events at Manus in the tropical west Pacific. Additionally, Bellenger et al. (2015) showed that moistening by shallow clouds during DYNAMO was preceded and followed by anomalous drying of approximately the same magnitude, so that net moistening in the shallow cloud layer was near zero.

7. Evolution of cloud updraft buoyancy entering transition periods

In the previous sections, we demonstrated that WRF simulates clear transition periods prior to MJO convective onset. We also concluded that evaporation within moderately deep cumulonimbi that were present during the transition periods was responsible for tropospheric moistening that presumably made the environment

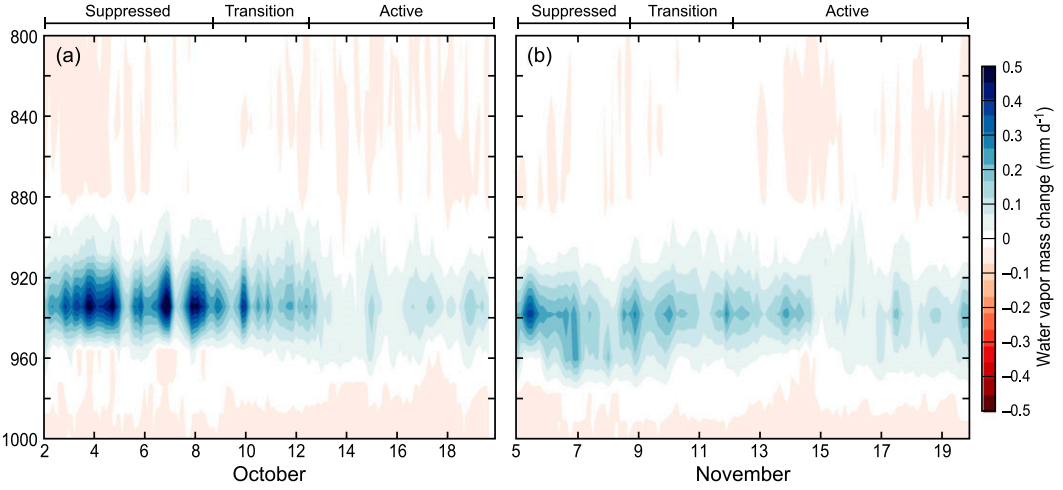

FIG. 12. Time series of total domain water vapor mass tendency attributed to nonprecipitating clouds for (a) October and (b) November.

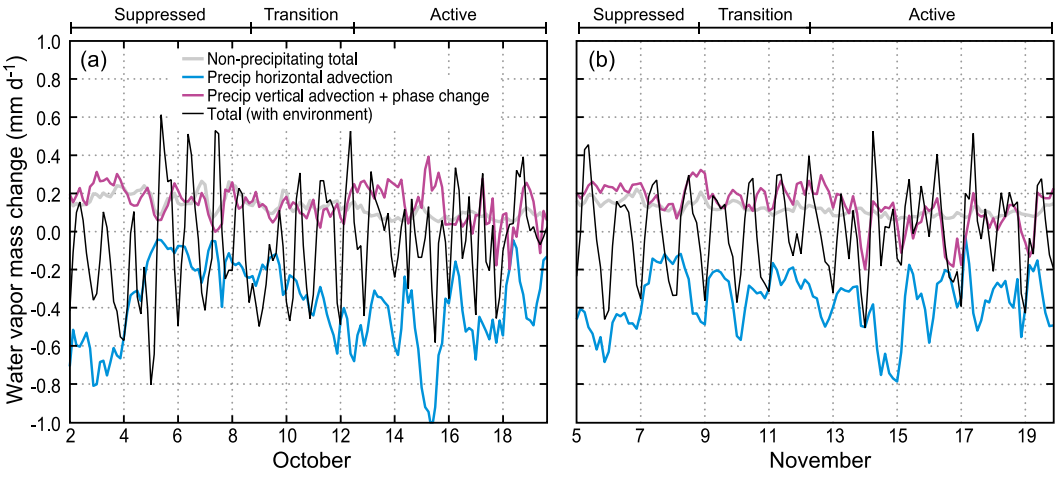

FIG. 13. Time series of total domain water vapor mass tendency attributed to nonprecipitating elements (gray), horizontal advection in precipitating elements (blue), vertical advection and phase changes in precipitating elements (magenta), and total tendency (black) in the 900–950-hPa layer during the periods (a) 2–20 Oct and (b) 5–20 Nov.

conducive to development of deeper convection. But what drove the observed and simulated rapid shift from a suppressed period with mostly shallow clouds present to a transition period during which moderately deep cumulonimbi were prevalent?

Because clouds have long been suspected of being the agents that moisten the environment prior to MJO convective onset, much of the study of cloud populations' evolutions on MJO-relevant time scales has focused on the evolution of the cloud depths. To a large degree, the vertical profiles of clouds' updraft buoyancies control their depths. A positively buoyant updraft is one that is less dense than its environment as seen from

$$B = -g\frac{\rho - \rho_0}{\rho_0}, \tag{3}$$

in which B is the buoyancy, $g = 9.81\,\mathrm{m\,s^{-1}}$, ρ is the cloud updraft density, and ρ_0 is the environmental density. Buoyancy can be directly impacted by changes in humidity, temperature, or hydrometeor content. By using the ideal gas law for moist air in which the virtual temperature T_v is substituted for temperature, one can easily arrive at the following estimate of in-cloud buoyancy:

$$B \approx g\left[\underbrace{\frac{T^*}{T_e}}_{\text{Temperature}} - \overbrace{\frac{p^*}{p_e}}^{\text{Pressure}} + \underbrace{0.608(w^*)}_{\text{Vapor}} - \overbrace{w_H}^{\text{Hydrometeor}}\right], \tag{4}$$

in which the subscript e represents a value in the environment surrounding a cloud updraft, and the superscript asterisk represents the difference between the in-cloud updraft value and the environmental value, T is temperature, p is pressure, w is mixing ratio, w_H is the hydrometeor (liquid water for the purposes of this study) mixing ratio, and virtual temperature T_v is approximated as

$$T_v \approx T(1 + 0.608w - w_l). \tag{5}$$

Figure 14 contains time series of mean buoyancy of cloud updrafts between 300 and 950 hPa. Updrafts are identified here as contiguous grid boxes in three dimensions that share the following properties: 1) they were part of precipitating clouds, 2) the rain-type classification of the column in which the updraft was identified as convective or isolated convective [following Powell et al. (2016)], and 3) vertical velocity in them was $\geq 0.3\,\mathrm{m\,s^{-1}}$. The second and third properties ensure that only fairly strong convective precipitation regions, and not stratiform or particularly weak convective regions, are included and the threshold is in the neighborhood of that used by LeMone and Zipser (1980) or Takemi (2015). In nature, strong convective updrafts have speeds that far exceed the threshold used herein; however, the use of 2-km grid spacing means that our simulations do not capture the most vigorous convective motions that occur on the order of tens to hundreds of meters. The updraft environment is defined as any environmental grid boxes within 10 km of an updraft. Defining the updraft environment as any points (i.e., precipitating and environment) within as little as 2 km or as much as 100 km of an updraft had no visible impact on our results, except that for the smallest values, some updrafts had very few or no clear-air grid boxes nearby. Using a different vertical velocity threshold

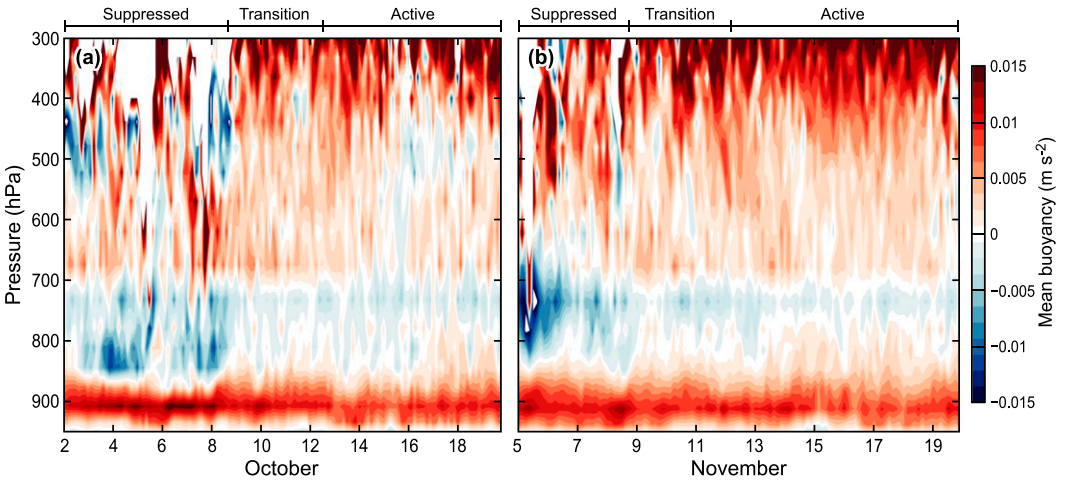

FIG. 14. Time series of the domain-averaged updraft buoyancy as described in the text during (a) October and (b) November.

(e.g., $1\,\mathrm{m\,s^{-1}}$ instead of $0.3\,\mathrm{m\,s^{-1}}$) also caused no noticeable change. Mean updraft buoyancy was often or always positive in the mean between about 850 and 950 hPa and negative in the 700–850-hPa layer. Updrafts were weakly positively buoyant in the mean between 700 and 550–600 hPa. Updraft mean buoyancy was also sometimes negative in October between 400 and 550 hPa. The layers of mean positive and negative buoyancy correspond respectively with less and more stable layers as described in section 1 and by Zuidema (1998).

At the beginning of the October transition period (9 October), and to a lesser extent near the start of the November transition period (9 November), the minimum mean negative buoyancy in the 700–850-hPa layer changed from roughly $-0.015\,\mathrm{m\,s^{-2}}$ during suppressed periods to $-0.005\,\mathrm{m\,s^{-2}}$ during transition periods. This is important because 700–850 hPa is directly above the nonprecipitating cloud layer, which was ubiquitous during suppressed periods and is the layer from which moderately deep cumulonimbi form. For both control simulations, Fig. 15 plots the contributions of each term in Eq. (4) to mean updraft buoyancy after their values at each model level in the 700–850-hPa layer are averaged together. The pressure term (gray) was small (0.002–$0.003\,\mathrm{m\,s^{-2}}$) in both simulations, and the hydrometeor term (magenta) hovered near -0.006 to $-0.007\,\mathrm{m\,s^{-2}}$ during both simulations. The magnitudes of the negative temperature term (green) and the positive humidity term (blue) were both usually in excess of $0.0075\,\mathrm{m\,s^{-2}}$ and $0.015\,\mathrm{m\,s^{-1}}$, respectively, prior to active MJO periods and largely balanced each other. Total mean updraft buoyancy in the 700–850-hPa layer (black) increased from roughly $-0.005\,\mathrm{m\,s^{-2}}$ 1–2 days before transition period onset to near zero right at the beginning of the October transition periods and from about 0 to about $0.025\,\mathrm{m\,s^{-2}}$ at the onset of the November transition period. In both months, mean updraft buoyancy in the layer remained slightly above zero throughout the transition period and after MJO convective onset. An increase in the domain-scale mean buoyancy suggests that updrafts entering the 700–850-hPa layer were more likely to penetrate through to the less stable layer above 700 hPa.

The particularly rapid increases in mean updraft buoyancy described above occurred on 8–9 October and 9 November. The sharp increases were accompanied by sharp increases in the temperature terms (green), which were partially offset by lesser decreases in the humidity terms (blue). In other words, while the mean 700–850-hPa environmental temperature was, on average, always greater than mean updraft temperature in the same layer, the difference between the two temperatures decreased quickly at the beginning of transition periods. Examining the temperature term in Eq. (4), and presuming a typical environmental temperature in this layer of 290 K, we see that an increase in mean updraft buoyancy of $\sim 0.12\,\mathrm{m\,s^{-2}}$ (seen on 8–9 October) or $\sim 0.007\,\mathrm{m\,s^{-2}}$ (seen on 9 November) respectively could have arisen from a change of only ~0.4 or ~0.2 K in the mean temperature difference between cloud environments and updrafts.

To help investigate this change, we plot in Fig. 16 the mean environmental (magenta) and updraft (blue) temperatures between 700 and 850 hPa, both of which exhibit significant diurnal variability. The environmental temperature decreased rapidly around 9 October after a slow warming trend. Updraft temperatures remained within the same range through the early portion of the October transition period. In November, environmental and

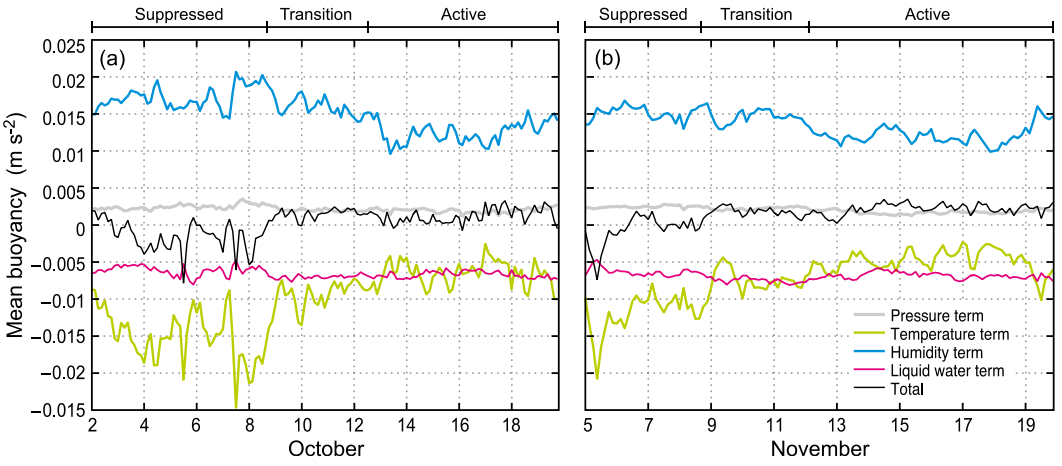

FIG. 15. Time series of the contributions to domain-mean updraft buoyancy in the 700–850-hPa layer by the pressure (gray), temperature (green), humidity (blue), liquid water (magenta), and sum of all (black) terms following Eq. (4) during (a) October and (b) November.

updraft temperature respectively trended slowly downward and upward for most of the simulation. The starts of both transition periods were accompanied by sharp decreases in environmental temperature (~0.7 K in each month) and less dramatic decreases in updraft temperature, which led to smaller differences between the two as discussed and shown above.

Temperature tendency can be described by the atmospheric thermodynamic equation as follows:

$$\frac{\partial T}{\partial t} = \underbrace{-\mathbf{u}_h \cdot \nabla T}_{\text{Advective}} \overbrace{- w\left(\frac{g}{c_p} + \Gamma\right)}^{\text{Adiabatic}} + \underbrace{\frac{J}{c_p}}_{\text{Diabatic}}, \qquad (6)$$

where $\mathbf{u}_h$ is the horizontal component of wind, w is vertical velocity, Γ is the lapse rate, and J is the heating per unit mass attributed to diabatic processes (e.g., latent or radiative heating/cooling). Figure 17 shows the mean values (smoothed as a 1.5-day running mean to reduce the magnitude of the diurnal cycle and highlight longer-term changes) of the adiabatic (magenta), diabatic (blue), and advective (green) terms in Eq. (6) in the 700–850-hPa layer for cloud environments during both control simulations. The total instantaneous temperature tendency at each 3-h output time is shown in black. Significant diurnal variability is again seen in the largely offsetting adiabatic and diabatic terms and, thus, also the total. Prior to 6 October (Fig. 17a), a decrease in daily mean total heating rate from about 1 to near 0 K day^{-1} is accompanied by a decrease in adiabatic warming from about 2 to 1 K day^{-1}. The adiabatic heating rate gradually increased as the transition period began, possibly as subsidence intensified outside the

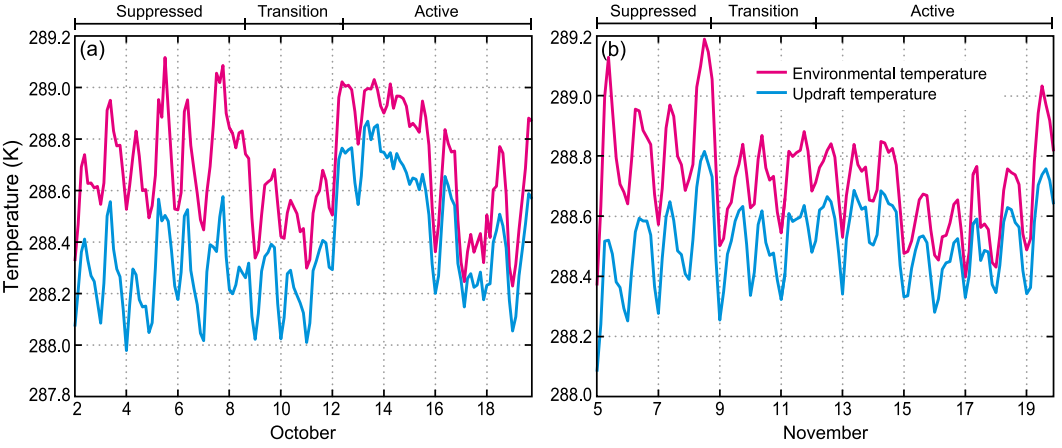

FIG. 16. Time series of domain-mean 700–850-hPa environmental (magenta) and cloud updraft (blue) temperatures during (a) October and (b) November.

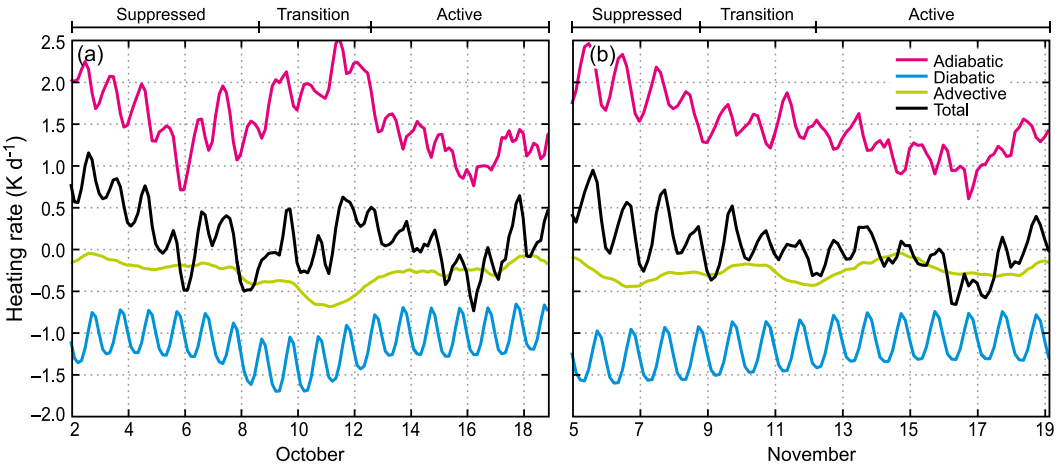

FIG. 17. Contributions to the domain-mean temperature tendency in cloud environments between 700 and 850 hPa, following Eq. (5), by adiabatic processes (magenta), latent plus radiative heating (blue), advection (green), and the total (black) during (a) October and (b) November. All time series are smoothed as a 1.5-day running mean to reduce the large magnitude of the diurnal cycle and highlight changes in each term over longer time periods.

deepening cloud population (Fig. 9f shows that the negative environmental vertical advection of moisture increased between 700 and 800 hPa when the October transition period initiated). An increase in daily mean diabatic cooling from about $-1.1\,\mathrm{K\,day^{-1}}$ on 6 October to $-1.4\,\mathrm{K\,day^{-1}}$ on 10 October accompanied a decrease in advective cooling from about $-0.2\,\mathrm{K\,day^{-1}}$ on 7 October to as low as $-0.7\,\mathrm{K\,day^{-1}}$ on 11 October. Furthermore, the sharpest decrease in environmental temperature on 8 October occurred during a diurnal minimum in diabatic heating, while the concurrent diurnal maximum in adiabatic warming barely recovered to $1.5\,\mathrm{K\,day^{-1}}$. All of these factors contributed to the extended period of total cooling that occurred at the beginning of the transition period on 8–9 October. In November (Fig. 17b), adiabatic (diabatic) heating rates gradually decreased (increased) during the simulation. The advective heating term oscillated between 0 and $-0.5\,\mathrm{K\,day^{-1}}$. The strong cooling at the beginning of 9 November again occurs during a diurnal minimum in diabatic heating, but it was again the gradual and steady decrease in daily mean adiabatic heating that set the stage for negative total environmental heating rates.

8. Conclusions

Recent studies have indicated that clouds drive moistening of the lower to middle troposphere, and it is presumed that because deep convection is sensitive to midtropospheric humidity (section 1), the development of these clouds is essential for MJO convective onset to occur. This article details the results of a modeling study that explores how cumulonimbus clouds moisten the troposphere below 400 hPa over the Indian Ocean prior to two MJO cases observed during DYNAMO in late 2011 and what processes cause cumulus clouds to more frequently deepen into moderately deep cumulonimbi during transition periods that occur in the days just preceding onset.

Our simulations perfectly replicated neither the timing nor location of convection over the ocean; however, they did produce three distinct modes of convection (shallow, moderately deep, and deep) that agree with observed distributions of real convection. The model also produced distinct transition periods (e.g., Powell and Houze 2015a,b) prior to MJO convective onset, during which moderately deep convection was prevalent. It was during these transition periods that the low to midtroposphere was moistened. Understanding MJO convective onset, at least for cases with preonset changes in the cloud population similar to that seen during DYNAMO, requires understanding of what causes transition periods to occur. Of course, the forcing and physics used for our simulations are not perfect, and we do not claim to definitively quantify the exact processes that caused MJO convective onset during DYNAMO. However, the model results are consistent enough with recent observations of the large-scale circulation and cloud population leading up to MJO convective events (section 3) to provide some insight into important mechanisms responsible for deepening the cloud population.

Our conclusions based on WRF simulations are summarized as the following:

1) The ceasing of net low-level moisture divergence that was present during suppressed periods, combined with moisture flux from the surface, ensured

that net vapor transport into the domain was positive during transition periods. Without surface moisture fluxes, total moisture tendencies would have usually been near or only slightly above zero in the region of MJO convective onset. However, variability in mean surface moisture flux over large areas was negligible and plays no role in determining when MJO convective onset occurs (Fig. 7).

2) During transition periods, a small positive residual of in-cloud moisture was present between 500 and 800 hPa. In other words, net condensation did not completely cancel out the in-cloud vertical flux of moisture. This residual was due to in-cloud evaporation, which was associated with either detrainment of moisture into the environment or eventual dissipation of clouds. Horizontal advection of moisture in the immediate environment of simulated clouds was an additional important moistening effect (Figs. 9–11).
3) Shallow, nonprecipitating convection between 900 and 950 hPa played a minimal role in net moistening of the troposphere prior to MJO onset. While such shallow convection had a moistening effect, its humidification was balanced by drying via subsidence in the environment and drying by horizontal advection in precipitating elements in the layer where nonprecipitating clouds were present. In the model, clouds with tops higher than 900 hPa were at least lightly precipitating, but some such clouds that extended slightly above 900 hPa probably correspond to nonprecipitating clouds in nature and may have small impacts on moistening at the levels where they exist. The potential impact of such clouds was not separately quantified in this study (Figs. 12 and 13).
4) Whether shallow cumuli developed into moderately deep cumulonimbi depended on their updrafts' buoyancies relative to their environments between 700 and 850 hPa. Reductions of mean environmental temperature and/or an increase in mean updraft temperature were the main factors that allowed an updraft to become more buoyant. Changes in the difference between the two of less than 0.4 K were enough to have major effects on the ultimate depth of an updraft. Environmental temperature rapidly decreased at the beginning of transition periods prior to MJO onset because of an increase in cooling driven by advection and radiation (in October) or a decrease in large-scale subsidence (in November). While the onset of transition periods appeared to be episodic and abrupt, the gradual reduction of large-scale subsidence near the end of suppressed periods in both simulations was first essential for reducing the environmental heating rate and for slowing the warming of the 700–850-hPa layer (Figs. 14–17).

Our fourth point above is at least roughly consistent with Tulich and Mapes (2010), who also demonstrated a strong sensitivity of tropospheric heating response to similarly small perturbations of tropospheric heating below the 0°C level in a cloud-resolving model. It may also be related to one of the major conclusions of Raymond and Fuchs (2007). They showed two types of unstable modes in a model for convectively coupled tropical disturbances. One of those was a ''gravity mode'' that propagated at about 18–19 $m\,s^{-1}$ and had a similar zonal structure to an equatorial Kelvin wave. Precipitation in that mode was partially controlled by changes in the convective inhibition in the 700–850-hPa layer [also shown by Herman et al. (2016)], just like in this article. Its eastward propagation speed also fell in the range of observed propagation speeds for a Kelvin wave–like circulation anomaly associated with the MJO as shown in Powell and Houze (2015a).

By quantifying changes in cloud updraft buoyancy prior to MJO onset, we have only explored one important factor that determines the ultimate depth of clouds. Entrainment of dry environmental air and in-cloud diabatic processes also contribute to updraft acceleration in individual clouds. However, our argument is not one that depends on the behavior of individual updrafts but rather is one that depends on the aggregate behavior of an ensemble of cloud updrafts over a large area and the relationship of updrafts to the environment in which they grow. Changes in the large-scale environment represent one means through which such aggregate behavior evolves. What we have argued herein is a method through which large-scale processes feedback onto cloud-scale processes. The cloud-scale dynamics are not quantified at the detail needed to evaluate the behavior of individual cloud elements, but our conclusions strongly suggest that the sum of cloud-scale processes over many cumuli scattered throughout the central Indian Ocean interact with large-scale dynamics and that such an interaction is necessary for MJO convective onset.

Tropospheric moistening is one major process that directly leads to MJO convective onset. This study takes another step back and explores the mechanisms responsible for the moistening. Our current results highlight the likely importance of processes occurring in the large-scale environment to deepening of clouds, agents of the tropospheric humidification. This is critically important because, while we can roughly hindcast an MJO using forcing that is somewhat anchored to observations, our ability to forecast MJO events is currently inadequate. Our results suggest that the ability of a free-running model to simulate a convectively active MJO depends on its ability to forecast large-scale

environmental flow and perhaps boundary layer temperature accurately over the tropical warm pool. Our results further stress the importance of evaporation of cloud condensate to tropospheric humidification, so for models that include a cumulus parameterization, interactions between clouds and the large-scale environment (e.g., cloud entrainment and detrainment) become critically important. Previous studies (Del Genio et al. 2012, 2015) have already shown the sensitivity of MJO predictability in a general circulation model to cumulus entrainment. Large-scale and cloud-scale dynamics are inseparable because the environmental flow impacts the properties of the air being entrained into updrafts. Also, the clouds themselves detrain moisture into their environments, a process that can be implied by this study but not directly quantified because of our coarse spatial resolution. Additionally, because the simulated transition periods are shorter than observed, the currently reported rates of simulated evaporative moistening should be considered with caution.

Not all MJO events are preceded by transition periods with durations like the ones observed during DYNAMO. Many others have been preceded by longer periods of time during which several episodic and temporary increases in convective depth were observed (Xu and Rutledge 2016). It is likely nonetheless that some of our results can be generalized to all MJO convective events. Particularly, something must always occur to allow mean updraft buoyancy above the nonprecipitating cloud layer to increase before widespread deep convection can occur. What cannot yet be generalized is what that ''something'' is. Powell and Houze (2015a) proposed a mechanism for convective deepening associated with circumnavigating disturbances that drives a reduction in large-scale subsidence—thus allowing clouds to deepen. Results for both simulations agree that gradual decreases in large-scale subsidence enhance vertical cloud development, but our October simulation especially suggests that processes occurring on shorter time scales might be important to trigger exactly when vertical development of a cumuliform population occurs. In general, any mechanism that allows for extended periods of favorable large-scale environmental conditions might lead to MJO convective onset. The range of such potential mechanisms should be explored further using reanalysis for past cases and, if possible, extensive in situ observations of clouds and the outside-of-cloud large-scale environment in future field experiments.

Acknowledgments. Beth Tully refined the graphics. Computing resources for running WRF were provided by the National Energy Research Scientific Computing Center (NERSC). The author was supported by grants from the Department of Energy (DE-SC0008452) and the National Science Foundation (AGS-1355567).

REFERENCES

Bellenger, H., K. Yoneyama, M. Katsumata, T. Nishizawa, K. Yasunaga, and R. Shirooka, 2015: Observation of moisture tendencies related to shallow convection. *J. Atmos. Sci.*, **72**, 641–659, doi:10.1175/JAS-D-14-0042.1.

Benedict, J. J., and D. A. Randall, 2007: Observed characteristics of the MJO relative to maximum rainfall. *J. Atmos. Sci.*, **64**, 2332–2354, doi:10.1175/JAS3968.1.

Bladé, I., and D. L. Hartmann, 1993: Tropical intraseasonal oscillations in a simple nonlinear model. *J. Atmos. Sci.*, **50**, 2922–2939, doi:10.1175/1520-0469(1993)050<2922:TIOIAS>2.0.CO;2.

Chikira, M., 2014: Eastward-propagating intraseasonal oscillation represented by Chikira–Sugiyama cumulus parameterization. Part II: Understanding moisture variation under weak temperature gradient balance. *J. Atmos. Sci.*, **71**, 615–639, doi:10.1175/JAS-D-13-038.1.

——, and M. Sugiyama, 2010: A cumulus parameterization with state-dependent entrainment rate. Part I: Description and sensitivity to temperature and humidity profiles. *J. Atmos. Sci.*, **67**, 2171–2193, doi:10.1175/2010JAS3316.1.

Ciesielski, P. E., and Coauthors, 2014: Quality-controlled upper-air sounding dataset for DYNAMO/CINDY/AMIE: Development and corrections. *J. Atmos. Oceanic Technol.*, **31**, 741–764, doi:10.1175/JTECH-D-13-00165.1.

Dee, D. P., and Coauthors, 2011: The ERA-Interim reanalysis: Configuration and performance of the data assimilation system. *Quart. J. Roy. Meteor. Soc.*, **137**, 553–597, doi:10.1002/qj.828.

Del Genio, A. D., Y. Chen, D. Kim, and M.-S. Yao, 2012: The MJO transition from shallow to deep convection in *CloudSat*/CALIPSO data and GISS GCM simulations. *J. Climate*, **25**, 3755–3770, doi:10.1175/JCLI-D-11-00384.1.

——, J. Wu, A. B. Wolf, Y. Chen, M.-S. Yao, and D. Kim, 2015: Constraints on cumulus parameterization from simulations of observed MJO events. *J. Climate*, **28**, 6419–6442, doi:10.1175/JCLI-D-14-00832.1.

Derbyshire, S. H., I. Beau, P. Bechtold, J.-Y. Grandpeix, J.-M. Piriou, J.-L. Redelsperger, and P. M. M. Soares, 2004: Sensitivity of moist convection to environmental humidity. *Quart. J. Roy. Meteor. Soc.*, **130**, 3055–3079, doi:10.1256/qj.03.130.

de Szoeke, S. P., J. B. Edson, J. R. Marion, C. W. Fairall, and L. Bariteau, 2015: The MJO and air–sea interaction in TOGA COARE and DYNAMO. *J. Climate*, **28**, 597–622, doi:10.1175/JCLI-D-14-00477.1.

Gottschalck, J., P. E. Roundy, C. J. Schreck III, A. Vintzileos, and C. Zhang, 2013: Large-scale atmospheric and oceanic conditions during the 2011–12 DYNAMO field campaign. *Mon. Wea. Rev.*, **141**, 4173–4196, doi:10.1175/MWR-D-13-00022.1.

Hagos, S., Z. Feng, C. D. Burleyson, K.-S. S. Lim, C. N. Long, D. Wu, and G. Thompson, 2014a: Evaluation of convection-permitting model simulations of cloud populations associated with the Madden-Julian Oscillation using data collected during the AMIE/DYNAMO field campaign. *J. Geophys. Res. Atmos.*, **119**, 12 052–12 068, doi:10.1002/2014JD022143.

——, ——, K. Landu, and C. N. Long, 2014b: Advection, moistening, and shallow-to-deep convection transitions during the initiation and propagation of Madden-Julian Oscillation. *J. Adv. Model. Earth Syst.*, **6**, 938–949, doi:10.1002/2014MS000335.

Herman, M. J., Z. Fuchs, D. J. Raymond, and P. Bechtold, 2016: Convectively coupled Kelvin waves: From linear theory to global models. *J. Atmos. Sci.*, **73**, 407–428, doi:10.1175/JAS-D-15-0153.1.

Hollars, S., Q. Fu, J. Comstock, and T. Ackerman, 2004: Comparison of cloud-top height retrievals from ground-based 35 GHz MMCR and GMS-5 satellite observations at ARM TWP Manus site. *Atmos. Res.*, **72**, 169–186, doi:10.1016/j.atmosres.2004.03.015.

Hsu, H.-H., B. J. Hoskins, and F.-F. Jin, 1990: The 1985/86 intraseasonal oscillation and the role of the extratropics. *J. Atmos. Sci.*, **47**, 823–839, doi:10.1175/1520-0469(1990)047<0823:TIOATR>2.0.CO;2.

Huffman, G. J., and Coauthors, 2007: The TRMM Multisatellite Precipitation Analysis: Quasi-global, multiyear, combined-sensor precipitation estimates at fine scales. *J. Hydrometeor.*, **8**, 38–55, doi:10.1175/JHM560.1.

Iacono, M. J., J. S. Delamere, E. J. Mlawer, M. W. Shepard, S. A. Clough, and W. D. Collins, 2008: Radiative forcing by long-lived greenhouse gases: Calculations with the AER radiative transfer models. *J. Geophys. Res.*, **113**, D13103, doi:10.1029/2008JD009944.

Janjić, Z. I., 1994: The step-mountain eta coordinate model: Further developments of the convection, viscous sublayer and turbulence closure schemes. *Mon. Wea. Rev.*, **122**, 927–945, doi:10.1175/1520-0493(1994)122<0927:TSMECM>2.0.CO;2.

Johnson, R. H., and P. E. Ciesielski, 2013: Structure and properties of Madden–Julian oscillations deduced from DYNAMO sounding arrays. *J. Atmos. Sci.*, **70**, 3157–3179, doi:10.1175/JAS-D-13-065.1.

——, T. M. Rickenbach, S. A. Rutledge, P. E. Ciesielski, and W. H. Schubert, 1999: Trimodal characteristics of tropical convection. *J. Climate*, **12**, 2397–2418, doi:10.1175/1520-0442(1999)012<2397:TCOTC>2.0.CO;2.

——, ——, J. H. Ruppert Jr., and M. Katsumata, 2015: Sounding-based thermodynamic budgets for DYNAMO. *J. Atmos. Sci.*, **72**, 598–622, doi:10.1175/JAS-D-14-0202.1.

Kingsmill, D. E., and R. A. Houze Jr., 1999: Kinematic characteristics of air flowing into and out of precipitating convection over the west Pacific warm pool: An airborne Doppler radar survey. *Quart. J. Roy. Meteor. Soc.*, **125**, 1165–1207, doi:10.1002/qj.1999.49712555605.

Knutson, R. R., and K. M. Weickmann, 1987: 30–60 day atmospheric oscillations: Composite life cycles of convection and circulation anomalies. *Mon. Wea. Rev.*, **115**, 1407–1436, doi:10.1175/1520-0493(1987)115<1407:DAOCLC>2.0.CO;2.

Kuang, Z., 2010: Linear response function of a cumulus ensemble to temperature and moisture perturbations and implications for the dynamics of convectively coupled waves. *J. Atmos. Sci.*, **67**, 941–962, doi:10.1175/2009JAS3260.1.

LeMone, M. A., and E. J. Zipser, 1980: Cumulonimbus vertical velocity events in GATE. Part I: Diameter, intensity, and mass flux. *J. Atmos. Sci.*, **37**, 2444–2457, doi:10.1175/1520-0469(1980)037<2444:CVVEIG>2.0.CO;2.

Madden, R. A., and P. R. Julian, 1971: Detection of a 40–50-day oscillation in the zonal wind in the tropical Pacific. *J. Atmos. Sci.*, **28**, 702–708, doi:10.1175/1520-0469(1971)028<0702:DOADOI>2.0.CO;2.

——, and ——, 1972: Description of global-scale circulation cells in the tropics with a 40–50 day period. *J. Atmos. Sci.*, **29**, 1109–1123, doi:10.1175/1520-0469(1972)029<1109:DOGSCC>2.0.CO;2.

Maloney, E. D., and B. O. Wolding, 2015: Initiation of an intraseasonal oscillation in an aquaplanet general circulation model. *J. Adv. Model. Earth Syst.*, **7**, 1956–1976, doi:10.1002/2015MS000495.

Posselt, D. J., S. C. van den Heever, and G. L. Stephens, 2008: Trimodal cloudiness and tropical stable layers in simulations of radiative convective equilibrium. *Geophys. Res. Lett.*, **35**, L08802, doi:10.1029/2007GL033029.

Powell, S. W., and R. A. Houze Jr., 2013: The cloud population and onset of the Madden-Julian oscillation over the Indian Ocean during DYNAMO-AMIE. *J. Geophys. Res. Atmos.*, **118**, 11 979–11 995, doi:10.1002/2013JD020421.

——, and ——, 2015a: The effect of dry large-scale vertical motions on initial MJO convective onset. *J. Geophys. Res. Atmos.*, **120**, 4783–4805, doi:10.1002/2014JD022961.

——, and ——, 2015b: Evolution of convective echo top heights observed by TRMM radar over the Indian Ocean and Maritime Continent during DYNAMO. *J. Geophys. Res. Atmos.*, **120**, 3906–3919, doi:10.1002/2014JD022934.

——, ——, A. Kumar, and S. A. McFarlane, 2012: Comparison of simulated and observed continental tropical anvil clouds and their radiative heating profiles. *J. Atmos. Sci.*, **69**, 2662–2681, doi:10.1175/JAS-D-11-0251.1.

——, ——, and S. R. Brodzik, 2016: Rainfall-type categorization of radar echoes using polar coordinate reflectivity data. *J. Atmos. Oceanic Technol.*, **33**, 523–538, doi:10.1175/JTECH-D-15-0135.1.

Rasmussen, K. L., and R. A. Houze Jr., 2016: Convective initiation near the Andes in subtropical South America. *Mon. Wea. Rev.*, **144**, 2351–2374, doi:10.1175/MWR-D-15-0058.1.

Ray, P., and T. Li, 2013: Relative roles of circumnavigating waves and extratropics on the MJO and its relationship with the mean state. *J. Atmos. Sci.*, **70**, 876–893, doi:10.1175/JAS-D-12-0153.1.

Raymond, D. J., and Z. Fuchs, 2007: Convectively coupled gravity and moisture modes in a simple atmospheric model. *Tellus*, **59A**, 627–640, doi:10.1111/j.1600-0870.2007.00268.x.

Ruppert, J. H., Jr., and R. H. Johnson, 2015: Diurnally modulated cumulus moistening in the pre-onset stage of the Madden–Julian oscillation during DYNAMO. *J. Atmos. Sci.*, **72**, 1622–1647, doi:10.1175/JAS-D-14-0218.1.

Skamarock, W. C., and Coauthors, 2008: A description of the Advanced Research WRF version 3. NCAR Tech. Note NCAR/TN-475+STR, 113 pp., doi:10.5065/D68S4MVH.

Takemi, T., 2015: Relationship between cumulus activity and environmental moisture during the CINDY2011/DYNAMO field experiment as revealed from convection-resolving simulations. *J. Meteor. Soc. Japan*, **93A**, 41–58, doi:10.2151/jmsj.2015-035.

Tewari, M., and Coauthors, 2004: Implementation and verification of the unified Noah land-surface model in the WRF model. *20th Conf. on Weather Analysis and Forecasting/16th Conf. on Numerical Weather Prediction*, Seattle, WA, Amer. Meteor. Soc., 14.2a. [Available online at https://ams.confex.com/ams/84Annual/techprogram/paper_69061.htm.]

Thompson, G., P. R. Field, R. M. Rasmussen, and W. D. Hall, 2008: Explicit forecasts of winter precipitation using an improved bulk microphysics scheme. Part II: Implementation of a new snow parameterization. *Mon. Wea. Rev.*, **136**, 5095–5115, doi:10.1175/2008MWR2387.1.

Tulich, S. N., and B. E. Mapes, 2010: Transient environmental sensitivities of explicitly simulated tropical convection. *J. Atmos. Sci.*, **67**, 923–940, doi:10.1175/2009JAS3277.1.

Ulate, M., C. Zhang, and J. Dudhia, 2015: Role of water vapor and convection-circulation decoupling in MJO simulations by a tropical channel model. *J. Adv. Model. Earth Syst.*, **7**, 692–711, doi:10.1002/2014MS000393.

Wang, B., 2011: Theories. *Intraseasonal Variability of the Atmosphere-Ocean Climate System*, 2nd ed., W. K.-M. Lau and D. E. Waliser, Eds., Springer, 335–398.

Wang, S., and A. H. Sobel, 2012: Impact of imposed drying on deep convection in a cloud-resolving model. *J. Geophys. Res.*, **117**, D02112, doi:10.1029/2011JD016847.

——, ——, A. Fridland, Z. Feng, J. M. Comstock, P. Minnis, and M. L. Nordeen, 2015a: Simulations of cloud-radiation interaction using large-scale forcing derived from the CINDY/DYNAMO northern sounding array. *J. Adv. Model. Earth Syst.*, **7**, 1472–1498, doi:10.1002/2015MS000461.

——, ——, F. Zhang, Q. Sun, Y. Yue, and L. Zhou, 2015b: Regional simulation of the October and November MJO events observed during the CINDY/DYNAMO field campaign at gray zone resolution. *J. Climate*, **28**, 2097–2119, doi:10.1175/JCLI-D-14-00294.1.

Xu, W., and S. A. Rutledge, 2014: Convective characteristics of the Madden–Julian oscillation over the central Indian Ocean observed by shipborne radar during DYNAMO. *J. Atmos. Sci.*, **71**, 2859–2877, doi:10.1175/JAS-D-13-0372.1.

——, and ——, 2016: Time scales of shallow-to-deep convective transition associated with the onset of Madden-Julian oscillations. *Geophys. Res. Lett.*, **43**, 2880–2888, doi:10.1002/2016GL068269.

Yoneyama, K., C. Zhang, and C. N. Long, 2013: Tracking pulses of the Madden–Julian oscillation. *Bull. Amer. Meteor. Soc.*, **94**, 1871–1891, doi:10.1175/BAMS-D-12-00157.1.

Zermeño-Díaz, D., C. Zhang, P. Kollias, and H. Kalesse, 2015: The role of shallow cloud moistening in MJO and non-MJO convective events over the ARM Manus site. *J. Atmos. Sci.*, **72**, 4797–4820, doi:10.1175/JAS-D-14-0322.1.

Zhang, C., 2005: Madden-Julian Oscillation. *Rev. Geophys.*, **43**, RG2003, doi:10.1029/2004RG000158.

Zhao, C., T. Li, and T. Zhou, 2013: Precursor signals and processes associated with MJO initiation over the tropical Indian Ocean. *J. Climate*, **26**, 291–307, doi:10.1175/JCLI-D-12-00113.1.

Zuidema, P., 1998: The 600–800-mb minimum in tropical cloudiness observed during TOGA COARE. *J. Atmos. Sci.*, **55**, 2220–2228, doi:10.1175/1520-0469(1998)055<2220:TMMITC>2.0.CO;2.